

Chapter 6

Closed Cell Systems for In Situ TEM with Gas Environments Ranging from 0.1 to 5 Bar

A.K. Erdamar, S. Malladi, F.D. Tichelaar, and H.W. Zandbergen

Abstract The ability to carry out reactions with gas mixtures in a TEM is becoming an increasingly important field of study, known as environmental transmission electron microscopy (ETEM). Different approaches exist to expose the material to a gas while imaging in a TEM: an open system employing differential pumping and a closed system using microelectromechanical systems (MEMS). The latter approach using electron transparent windows in a device holding the specimen and the gas came up during the last decade, enabling a gas pressure of several bars. Here, we present this closed cell approach based on a functional MEMS device known as “nanoreactor” to investigate gas–material interactions inside a TEM. We discuss the design and the development of different kinds of nanoreactors, along with the necessary accessories to carry out drift-stabilized, atomic-resolution environmental TEM studies. Finally, examples showing the applications of the nanoreactor to investigate several gas–liquid–material interactions are presented.

6.1 Introduction

TEM experiments are almost always performed with a 10^{-7} mbar environment around the specimen. This has to be done because the electrons have such a strong interaction with matter (and thus also gas molecules) that even a low gas pressure in the electron microscope results in a strong blurring of the TEM image. Over the last two decades, the development of environmental TEMs (ETEM) has made it possible to increase the pressure around the specimen while maintaining an acceptable vacuum in other parts of the TEM. This was realized by adding extra pumps and pumping apertures. A disadvantage is that the maximum pressure around the specimen for high-resolution imaging is about 10 mbar. This limitation is caused by

A.K. Erdamar (✉) • S. Malladi • F.D. Tichelaar • H.W. Zandbergen
Kavli Institute of Nanoscience, Delft University of Technology, Lorentzweg 1,
2628 CJ Delft, The Netherlands
e-mail: a.k.erdamar@tudelft.nl

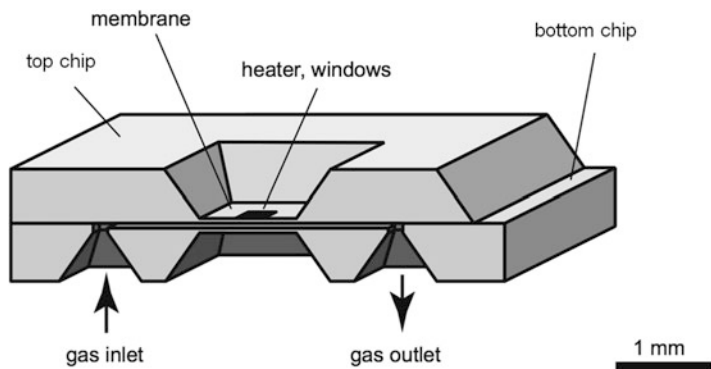


Fig. 6.1 Schematic presentation of a nanoreactor composed of two chips

the geometries in an ETEM. More than a decade ago, we realized that in order to do experiments at realistic pressures, it was necessary to develop a system with a shorter gas column. The gas column in an ETEM is about 10 mm and had to be shortened by several orders of magnitude to allow pressures of 1 bar and more. Practically, this shortening can be achieved best by developing a small microreactor or nanoreactor (NR) based on semiconductor production techniques. Figure 6.1 shows the design of the first type of NR (Creemer et al. 2008). Several prototype NRs have been designed and manufactured, which allowed getting atomic resolution images at 1 bar gas pressure and 700 °C.

6.2 The Nanoreactor Developments in Delft

The research in Delft employing MEMS to create a 1 bar environment around the sample started in 2001 with the use of a sandwich nanoreactor in which two MEMS-processed chips were aligned with respect to each other and fixed with a two-component glue. This type of ensemble was successfully used for various in situ experiments at 1 bar (Creemer et al. 2008). However, when we tried to use these glued NRs more routinely, it turned out that carbon contamination (C-contamination), ease of use (including making it airtight), and the yield were major bottlenecks.

Various routes have been explored to solve the C- contamination issue: (1) finding an organic-based glue that does not outgas, (2) using an inorganic glue (water glass) (Yokosawa et al. 2012), (3) using a Viton O-ring to make an airtight connection between the bottom and top chip, (4) making the NR as one complete chip (Creemer et al. 2011). Note that apart from the NR, contamination can also originate from hydrocarbon impurities in the rest of the gas system (in the holder and in the gas supply system). Several organic-based glues have been tried, but we could not find glue that did not result in C-contamination. Alternatively, water glass

(a solution of sodium metasilicate, Na_2SiO_3) has been used as glue. Being inorganic, it was possible to achieve C-contamination-free experiments several times, but achieving airtightness with this glue has been quite challenging. To solve the problem of possible leakage through water glass seal, the holder has been modified such that leakage through the interface between the two chips is not a problem for the vacuum of the TEM. A drawback of gluing the two chip halves is that once glued, it is nearly impossible to separate them. For this reason, we developed a third method for the sandwiched chip NR, where the sealing is achieved through O-rings without glue. In this design, the two chips are clamped together (see Sect. 6.4), but can be separated after the in situ TEM experiments to allow additional experiments on the same sample, for instance using a highly surface sensitive technique which requires the absence of the top chip. We have also developed an NR that consists of one component only (Creemer et al. 2011). One-chip and sandwiched chip NRs are similar in size and can therefore be loaded in the same holder.

Concerning the required vacuum tightness, the NRs and holders and their interfacings have to be vacuum sealed. Due to the very limited space in TEM holders, this is not a trivial task. For standard high vacuum connections, one normally uses O-rings of a shore diameter of 2–3 mm. But because of the space limitations in particular along the electron beam direction such O-ring sizes cannot be used. All the NR-holder components (lid, NR top, O-ring, NR bottom, O-ring, holder) have to fit within 2–3 mm. As a result, the O-rings must have a shore of about 0.40 mm. The typical tolerance for an O-ring of 0.40 mm is 0.08 mm, which is more than the tolerance of about 0.02 mm in compression of the O-ring needed for vacuum tightness. Thus, a careful selection and optimization of all components of the assembly is needed.

6.3 Different Types of Nanoreactors

Two major types of NRs (see Fig. 6.2) are used in Delft: the sandwiched chip NR and the one-chip NR consisting of a bottom chip with heater and top chip. Both types can be used in a static gas system, i.e., the gas must be loaded outside the TEM, and in a flowing gas system, i.e., the gas is led from a gas handling system outside the TEM through tubes in the TEM holder and through the NR and back. The sandwiched chip NR has two types of heaters: a spiral-shaped heater with electron transparent windows in between the Pt heater spiral, or a flat center heater with a larger area for specimen mounting. A brief comparison between both the NR designs is given in Table 6.1. Information on the fabrication of both kinds of NRs is given further in the chapter (Table 6.1).

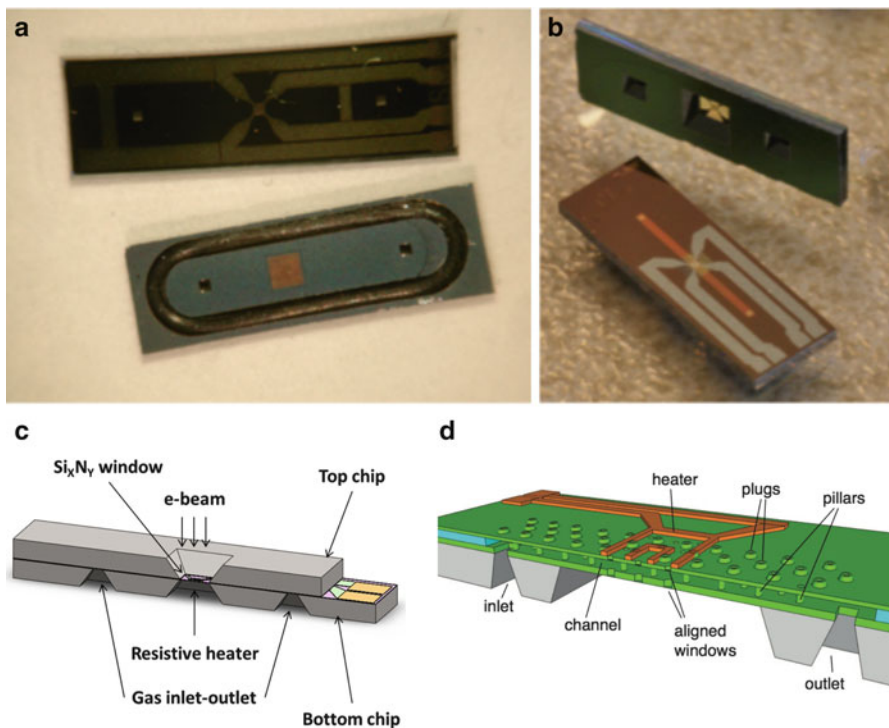


Fig. 6.2 Optical images of the two chip halves of the sandwich NR (a) and one-chip NR seen from top and bottom (b). (c) 3-D sketch of the sandwich NR, consisting of a bottom chip with the heater and the contact pads for connection of the heater to the heater control. (d) 3-D sketch of the all-in-one NR. For clarity, the thin-films' thicknesses have been drawn thicker than they are in reality. The channel is 4.6 mm long and 0.3 mm wide

6.4 The NR Holders Used in Delft

The NR has to be supported by a holder, whereby the combination of NR and holder should allow: (1) full vacuum tightness, (2) a resolution better than 1 Å, (3) reliable electrical contacts for the MEMS heater in the NR, and (4) a gas inlet and outlet in the case of the flowing gas holder.

Note that the gas tubes and the wiring for the electrical contacts have to fit into the TEM holder. This limits possible upgrades like adding valves in the tubes or preheating of the gas in the tube. Differences in the size of the holders influence the design of the NR. As an example, FEI and JEOL holders are shown in Fig. 6.3. Obviously, the JEOL holder with its much larger diameter provides more space for add-ons in the holder. Nevertheless, up till now we have always been able to realize all features in the FEI holders (with an inner bore of the narrow part of the holder tube being less than 5.5 mm) in which the most complicated one was a double tilt vacuum transfer heating-holder.

Table 6.1 Advantages (in *upright*) and disadvantages (in *italics*) of sandwiched chips and one-chip NRs

Sandwiched chips NR	One chip NR
Samples of any size can be loaded	<i>Only particles can be loaded with a dispersion led through the gas channel</i>
Sample can be positioned at a desired location (only in middle of heater)	<i>The whole inside space of the NR will contain particles</i>
Sample is only present on the heater membrane	Sample is present on both membranes
<i>Channel height can increase from 5 to 35 μm upon gas pressure.</i>	Channel height (e.g., 2 μm) independent on pressure
Top chip can be removed for further analysis (tomography, surface analysis, etc.)	<i>Top membrane cannot be removed</i>
<i>O-rings thickness between NR chips is critical</i>	NR itself is leak-tight
<i>Assembly process may cause contamination</i>	It is easier to prevent contamination
The fragile parts of the two chips are well protected	<i>Top of the chip is very fragile</i>
<i>Alignment of two chips could fracture a membrane</i>	Alignment is not an issue in this case
A modification (e.g., add biasing line) is fairly easy	<i>Modification is complicated</i>
More than one sample can be loaded and studied at the same time	<i>The loading of the suspension could clog the channel</i>
An NR can be used several times, e.g., in case of metal lamella	<i>Reusing this system also requires thorough cleaning which is not feasible in all cases.</i>
<i>External dirt particles can be present during the assembly</i>	Dust particles is limited to the suspension only

**Fig. 6.3** A comparison of the shapes of a JEOL and an FEI flowing gas holder

Figure 6.4 shows our latest flowing gas holder for an FEI TEM, which has been used for the 1 bar corrosion experiment discussed in Sect. 6.10.3. The gas system (all components that are in contact with the gas that is lead through the NR) can be taken out of the holder for dedicated cleaning. We used two types of materials for this: Pt and Ti. In the example shown in Fig. 6.4, the material is Ti. The construction

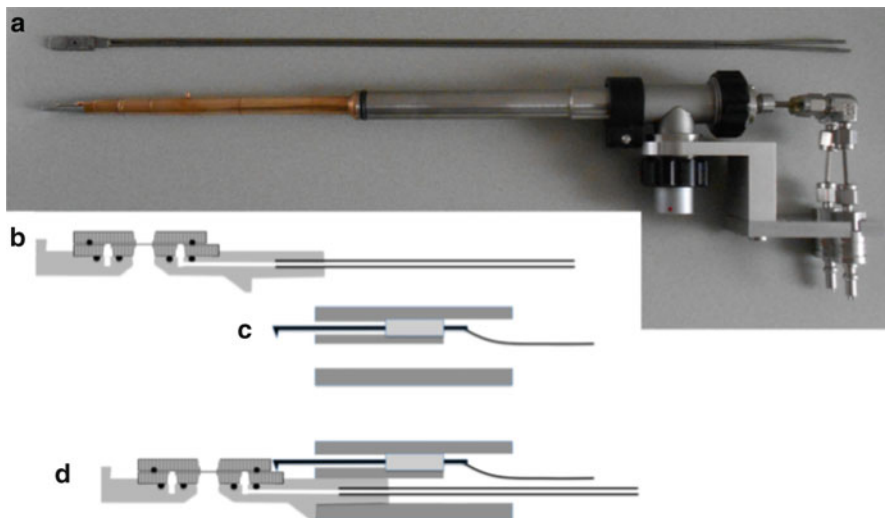


Fig. 6.4 The flowing gas holder (a) shows a holder that has been realized and has been used for corrosion experiments. Above the holder the tip/tubing combination is shown that can be removed as one piece. (b–d) Cross-sectional sketches of the holder tip disassembled and assembled onto the holder. The inlet and outlet tubes run all the way to the other side of the holder (extending outside of the TEM), where they are attached to a gas supply system. The tip and gas tubes of the holder shown in (a) are completely composed of Ti (except for the *O-rings* in the tip). This tip-tubes system can be taken out from the holder and be cleaned, for instance by a bake-out in vacuum at 300 °C

on the right side of the holder shown in Fig. 6.4 is to prevent strain on the Ti tube coming out of the holder, which could induce a leak due to the creep of the tubes.

Figure 6.5 shows our static gas holder. The holder has a separable tip, which contains an airtight chamber that can store gas with a volume of 1–10 mm³. Gas is loaded in or pumped out through a valve in the tip (see *arrow* in Fig. 6.5b). The NR is similar to that of the flowing gas holder, but could also be made more dedicated, for instance with a build-in pressure meter. In the experiments we did up till now, we used our standard NRs, which allow both static and gas-flow experiments.

Figure 6.6 shows a previously used holder, in which the NR is allowed to be leaky between the two chip halves. The advantage is that this connection between the two chips is not critical in the airtightness, for instance allowing glues that are not sealing very well but do not contain hydrocarbons. The disadvantage is that the lid (with a hole of 1.0 mm over the membrane area) to make the chamber in which the NR is located has been thick because the large O-ring has to be pressed down everywhere sufficiently by two screws of the far ends of the lid.

Some advantages and disadvantages of the static gas holder and the flowing gas holder are indicated in Table 6.2.

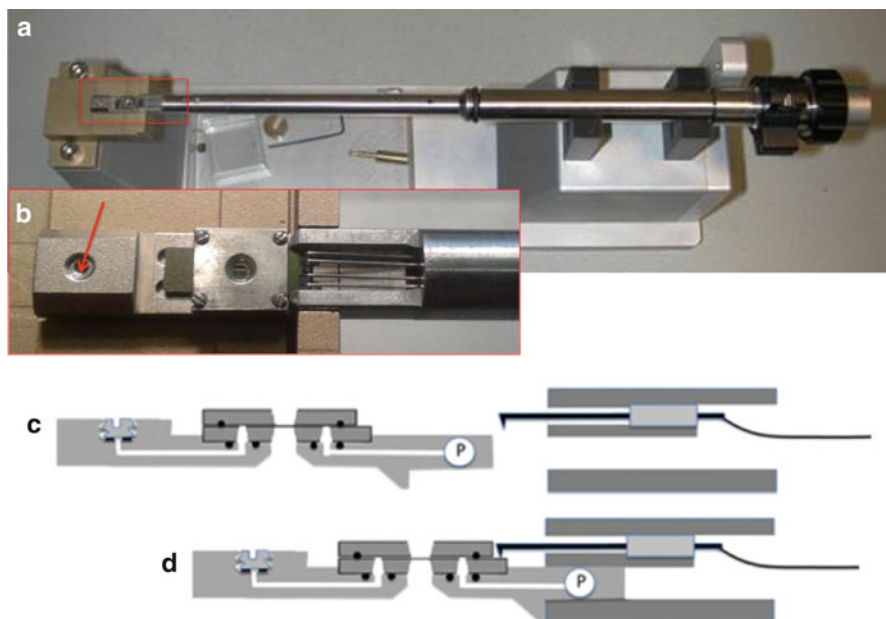


Fig. 6.5 (a) Image of the static gas holder and (b) an enlarged view of the tip part with the square lid on top. The red arrow indicates the valve to open or close the tip, (c, d) show cross-sectional sketches of the holder tip disassembled and assembled onto the holder, respectively. *P* indicates a pressure meter. The lid to clamp the two chips together is not given in (c) and (d) but can be seen in (b)

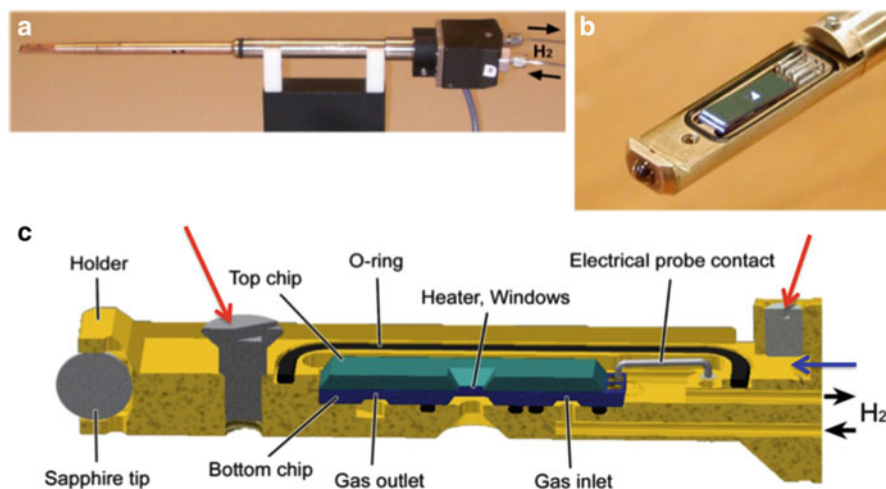


Fig. 6.6 Sample holder used for the 4.5 bar hydrogen gas experiments. (a) Sample holder. (b) NR inserted in the sample holder. The lid of the holder is removed for a better view. Mounting of the lid is done by sliding it into an opening indicated by the blue arrow and next tightening the screws indicated by the red arrows. (c) Schematic diagram of the NR inserted in the sample holder

Table 6.2 Comparison of using NR with static gas or flowing gas, advantages (in *upright*) and disadvantages (in *italics*)

Flowing gas system	Static gas system
<i>Gas handling system near TEM is complicated</i>	Simple setup at the TEM
Gas pressure regulation possible	<i>Pressure cannot be regulated, is dependent on T, and may drop due to leakage</i>
Alternating different gases possible	Because price of tip is small compared to whole holder, running several experiments in parallel (e.g., ageing) is well doable
Allowed leakage can be much higher than in static gas situation	<i>Even a very small leak results in significant pressure drop</i>
	Tiny gas volume allows for special/expensive gases
<i>High hazard gases not possible</i>	Also high hazard gases can be loaded outside the TEM area.
	Transfer to another analysis tool is easy
	Because price of tip is small compared to whole holder, running several experiments in parallel (e.g., ageing) is well doable

6.5 The Alignment Tool

The windows of the top and bottom chip have to be aligned to allow investigation of a sample on top of one of the windows by TEM. This is feasible with the alignment tools shown in Fig. 6.7. Two NR halves are placed on top of each other in the central part of the alignment tool. Next, the lid is placed on top of it. From this point on, two methods can be used. Method 1 involves (1) Slight tightening of the lid, (2) Alignment of the top chip to the bottom chip with micromanipulators, and (3) Further tightening of the lid. Method 2 consists of (1) Slight tightening of the lid-NRs ensemble with the block shown in Fig. 6.7b, (2) alignment of the chips, (3) tightening of the block, and (4) tightening of the lid with the four screws. The advantage of the latter method is that the force to the lid-NRs ensemble is mainly vertically applied which is important to prevent a breakage of one of the chips due to torsion. For the alignment, one needs a good optical microscope that allows clear imaging of the electron transparent windows (see also Fig. 6.18e). In general, one can see that the two membranes of the NR halves are close to each other using Newton rings.

6.6 The Gas Supply Systems in Delft

An important component of the NR in situ TEM experiments is the gas supply system. In the case of the static gas holder (see Fig. 6.8), loading the NR with the gas of interest is relatively straightforward. The tip of the holder is placed in an

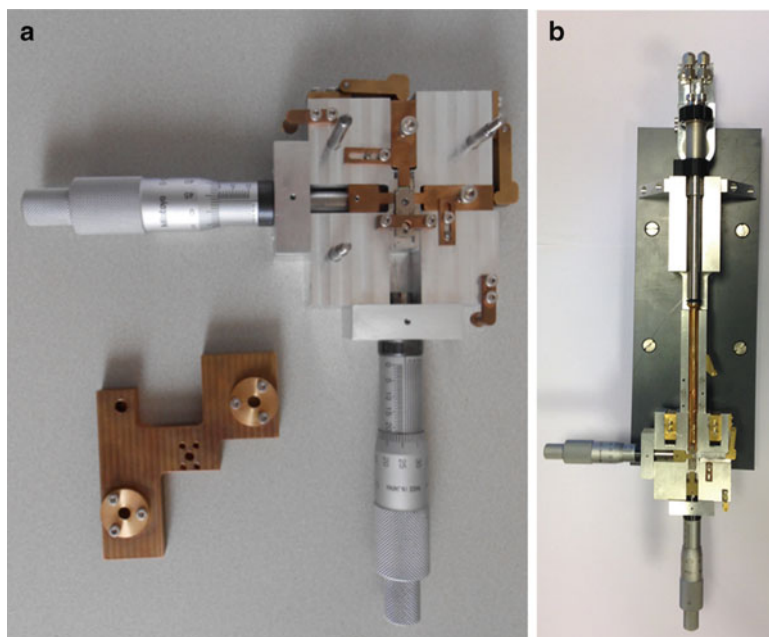


Fig. 6.7 (a) The alignment tool for a static gas holder. (b) The alignment tool for a gas-flow holder. The latter alignment tool is much larger because the holder has to be supported in one direction

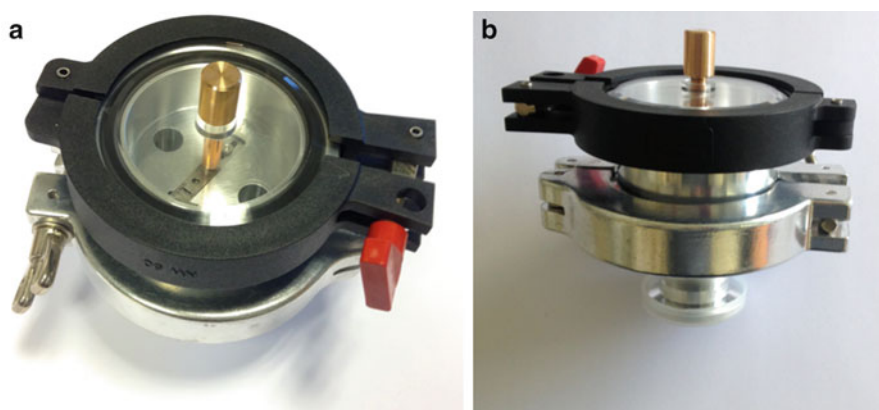


Fig. 6.8 The gas loading system seen from the *top* (a) and the *side* (b). The tip can be seen through the glass slide. The screw in the tip, acting as an airlock can be tightened (*closed*) or loosened (*open*), with the screw driver. The system has a standard NW16 connection at the bottom

enclosure. The valve in the tip is then opened and the chamber along with the NR is evacuated. Subsequently, the reactive gas of interest is introduced into the chamber at the pressure required for the in situ TEM study (typically 1 bar). The tip is left in

this configuration with the valve open for duration of 30 min to load the NR with reactive gas and the valve is then closed. This relatively long time is preferred because the gas has to travel to the gas chamber part through a thin gap in the NR. The NR is now set up for in situ TEM investigation. The handling becomes slightly more sophisticated when the flow-gas holder is used. The primary requirements for a successful in situ gas-flow experiment are a continuous gas supply at a constant pressure and a constant pressure on the outlet side of the NR. An inlet gas should be very clean to avoid any contamination during the investigation. More importantly, the gas supply system should account for all the safety standards by using a protective mechanism. This system shuts down the gas supply instantaneously in case of damage to the NR by reducing the gas leakage into the column to a minimum. Note that the NRs operate at nominal pressures of a few millibars to as high as 4.5 bar. Also, it is sometimes necessary to have a mixture of a gas and liquid (aerosols). Considering all these factors, different gas-flow systems for gases as well as aerosols have been developed.

Figure 6.9a shows the flow diagram for a gas supply system that allows multiple gas sources (currently three, but it can be modified to more gas sources). The front panel of this gas supply system is shown in Fig. 6.9b, which has been divided into a part for gas pressures lower than 2 bar and another part for gas pressures higher than 2 bar. This gas supply system has been assembled from a cuboidal framework of aluminum pillars to which the gas bottles are securely fastened with a front panel of aluminum sheet fitted with standard Swagelok valves and pressure gauges. All the tubes and components that come into contact with flowing gas are made of low-carbon stainless steel tubes. This assures corrosion resistivity against most of the commonly used gas mixtures like, e.g., H_2 , O_2 , CO, and CO_2 . As indicated in the flow diagram (Fig. 6.9a), the gas bottles are connected to a flow tube through a series of check valves, three-way valves, and toggle valves. The three-way valves divide the gas-flow system to a low-pressure part and high-pressure part. Both parts are essentially identical; the main difference is the presence of different filters in each section. Depending on the experimental requirements, the system can be operated either at high pressures or at low pressures by the flick of a switch. The system allows the choice of either a single gas or a mixture of two or three gases. In order to avoid the contamination of the gas bottles by other gases, check valves allowing unidirectional flow only have been fitted before the gas enters the mixing tube. A relief valve and a manometer monitoring the pressure of the gas after the mixing tube have been added as a safety mechanism in case of an excess pressure. Any residual moisture due to condensation in the tubes is detrimental to the TEM investigation. Therefore, the gas mixture flows through a charcoal filter and a needle valve before entering the TEM holder. The pressure behind this filter is monitored by a digital manometer, and its value is considered to be the pressure on the inlet of the NR.

A membrane pump is used to flow the gas and to maintain pressure differences between the inlet and the outlet of the holder. The outlet of the holder is connected to the membrane pump through a toggle valve, whereas the remainder of the gas

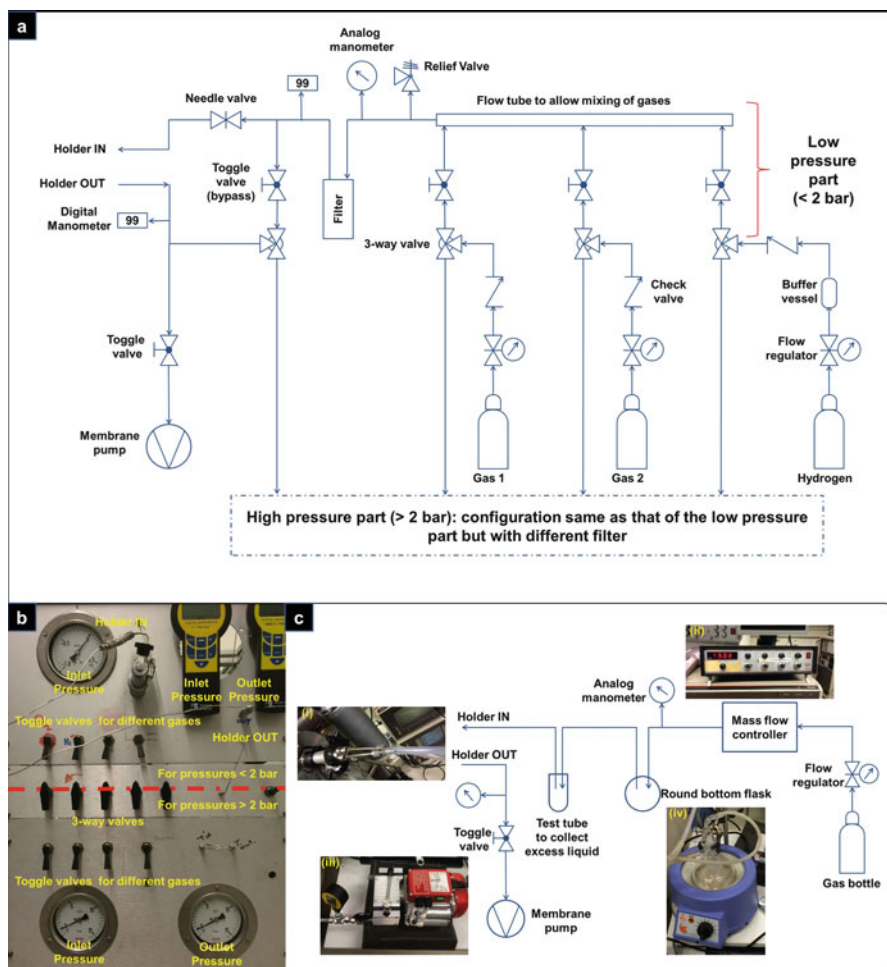


Fig. 6.9 Schematic representation of the gas supply system for the gas-flow holder (a) flow diagram for gas supply system allowing multiple gas sources, (b) front panel of gas supply system, (c) simplified version of gas flow system for reaction mixtures

supply system is connected to this pump through a three-way valve and a toggle valve (a bypass valve). The bypass valve connects the inlet part of the gas supply system (which is maintained at higher pressure) to the outlet part of the gas supply system. The outlet part is at a low pressure, typically around 15 mbar, determined by the membrane pump. When the bypass valve is open, the gas does not enter the TEM holder, which adds to additional safety of the microscope by preventing any excess gas leakage into the column.

In short, if the system is operational under pressures of 2 bar as shown in the figure, the experimental sequence is as follows: (1) Connect the TEM holder to the gas supply system and switch on the membrane pump with the bypass valve open; (2) Once the pressure on the digital manometers on the inlet and outlet has reached

almost the same value (this indicates the gas supply system is nearly evacuated), close the bypass valve to pump through the holder; (3) By carefully regulating the toggle valves and the needle valve before the inlet, it is possible to maintain a constant pressure difference between the inlet and the outlet of the holder.

Sometimes for certain in situ experiments, it is necessary to use aerosols, like in the case of aluminum alloys, where the corrosion in oxygen bubbled through aqueous HCl is studied. In certain cases, gases like H₂S are required. When such corrosive gases or aerosols are used, it is necessary to avoid contamination of the gas-flow system or to prevent the corrosion of stainless steel components. As an alternative, the gas supply system shown in Fig. 6.9c can be used. For aerosols, the carrier gas flowing from a bottle is regulated through a flow meter, which bubbles through a glass flask containing the solution of interest (typically aqueous). This creates an aerosol enriched with extremely fine droplets of the solution. Prior to the inlet tube of the holder, there is a test tube with two disconnected tubes, which acts as a sink for any excess liquid. The outlet of the holder is connected to the membrane pump through a toggle valve, and the pressure on the outlet is monitored. Likewise, the pressure on the inlet is monitored and regulated through the needle valves of the mass-flow controller.

6.7 Manufacturers of Nanoreactor Systems

There are three major companies that produce holders and chips for different types of in situ TEM experiments at pressures that cannot be realized in an ETEM: DENSsolutions (Guo et al. 2006), Hummingbird (Jenichen and Engler 2009), and Protochips (López Nieto et al. 2003).

The Hummingbird gas holder provides single and multichannel gas delivery systems, which are used to study solid–gas interactions at or just above atmospheric pressure. When the holder is fitted with a heating chip, it also supports real-time observation of catalysis reactions in the TEM. The sample can be heated up to ~800 °C. The temperature is controlled with closed-loop temperature control software that works with the calibrated sensor on the chip. Protochips has gas and liquid flow holders, giving the opportunity to study the real-time material behavior inside the TEM at pressure and temperature up to 1 bar and 1000 °C, respectively. Note that the presence of a gas allows heat exchange with its environment. When the temperature calibration was done in vacuum, this leads to wrong temperature indications (see further information below). Most of our own NR developments described in this chapter are or will be commercialized by DENSsolutions (He and Hull 2012). Several examples of applications of the gas holders are: (1) The solid–gas interactions related to oxidation reaction of cobalt-based nanocatalysts uncovering in situ evolution of the Kirkendall effect (Xin et al. 2013); (2) The oxidation of two-dimensional Ti₃C₂, also known as “Mxhene,” whereby the production of carbon-supported TiO₂ was shown as a function of the heating rate, the temperature range, and the exposure time (Ghassemi et al. 2014);

(3) The formation of mesoporous Pd powder with a pore diameters of 7 or 13 nm in vacuum and H₂ gas; (4) The (de)hydrogenation of Pd at pressures up to 4.5 bar (Yokosawa et al. 2012).

The three companies also have or will soon have liquid (flow) holders, which enable research to be carried out in a static or dynamic liquid environment, also see review by the de Jonge and Ross (2011)

Examples of this kind of in situ TEM are (1) in situ quantification of the electrochemical nucleation and growth of copper clusters on gold from a 0.1 M CuSO₄·5H₂O 1 vol.% H₂SO₄ solution (Radisic et al. 2006); (2) direct observation of calcium carbonate crystal nucleation which enables future research on the role of living organisms on this type of nucleation (Nielsen et al. 2014); (3) the use of ETEM in closed liquid cells or in liquid flow devices. The authors claimed that atomic resolutions can be achieved in liquid enclosures with 50 nm thick SiN membranes (de Jonge et al. 2014); (4) the electrochemical charging of a battery in a TEM liquid flow cell by imaging of electrochemically active ions in the electrode and electrolyte in electrical energy storage systems at nanoscale (Holtz et al. 2014); and (5) the structural evolution and electrochemical response of Pt–Fe nanocatalysts, which showed that the particles growth rate depends on both site and the potential (Zhu et al. 2014).

6.8 Design Requirements for the Nanoreactors

Several general requirements can be listed for the NRs:

1. The windows of the NRs must be sufficiently electron transparent, on the one hand, and able to withstand the applied pressure on the other hand.
2. The NR should allow heating of the gas and the specimen with a high accuracy in temperature.
3. The NR should allow straightforward loading of the specimens.
4. The NR should allow a controllable gas or liquid flow.
5. The NR and the holder should not be in conflict with normal TEM operation.

Furthermore, a few more specific requirements can be given:

6. The NR should be relatively easy to operate.
7. The carbon contamination should be negligible.
8. The electron transparent membranes of the NR should be uniform in thickness and amorphous.
9. The length of the gas or liquid column along the e-beam direction should be small (matching the required resolution).
10. It is preferable to have the resolution the same as that of the standard holder.
11. The drift should be small enough to record high-resolution images.

6.8.1 Requirement 1: Electron Transparent Windows that Withstand 10 bar

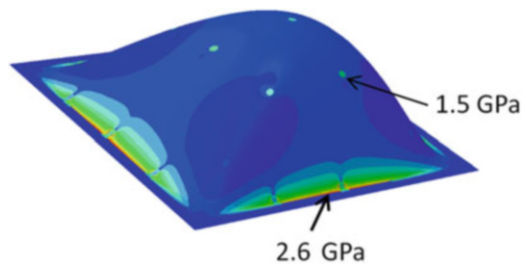
An MEMS NR consists of two parallel membranes of about 500 nm thick with a gas in between them. These two membranes contain several ultra-thin regions (e.g., 15 nm thick) that act as electron transparent windows. Most of the time we and other NR developers have used SiN as membrane material, but other materials such as SiC and SiO₂ are also possible. In this subsection, we write SiN membrane, but it should be read as a class of materials that are relatively inert, can withstand high temperatures, and are preferably amorphous.

When the goal is to obtain a gas pressure of 10 bar, the requirement for a reliable NR is that the big relatively thick membrane and the very thin electron transparent windows must survive exposure to this gas pressure. Modeling can be done on the mechanical response of different window geometries under uniform pressure to determine the limits of various designs. Furthermore, Alan et al. (2012) did an experimental study to characterize the reliability of certain window thicknesses. The simulations and the experiments show that high-pressure operation can easily be obtained by simple design rules for the SiN membranes and windows.

Nonlinear finite element ABAQUS software was used to map the deflections and stress distributions for the membranes under the influence of 10 bar uniform pressure to estimate the failure probability of the devices. Two components have to be modeled: (1) The larger membrane that contains, e.g., the microheater and (2) the electron transparent windows. The stress distribution in the large membrane is shown in Fig. 6.10. It can be seen that the largest stress is present near the location, where the membrane is attached to the Si chip. Note that these stresses can be reduced by changing the size and shape of the windows which is discussed in Fig. 6.12. In addition to larger membrane calculations, several different window geometries (elongated and circular) were tested as illustrated in Fig. 6.11 and Table 6.3. The maximum stress values decrease with decreasing lateral dimensions. Circular structures have lower maximum stresses, due to their symmetry.

Next, the simulations were repeated by taking the corner stress singularities into account. Figure 6.12 shows the models for two calculations: a 90° corner and a tapered shape. The calculations show that the tapered corner has reduced stresses (from 2.85 to 1.95 GPa), and hence increases reliability significantly.

Fig. 6.10 Stress distribution in the large membrane and the electron transparent circular SiN windows (small green areas, one indicated by an arrow)



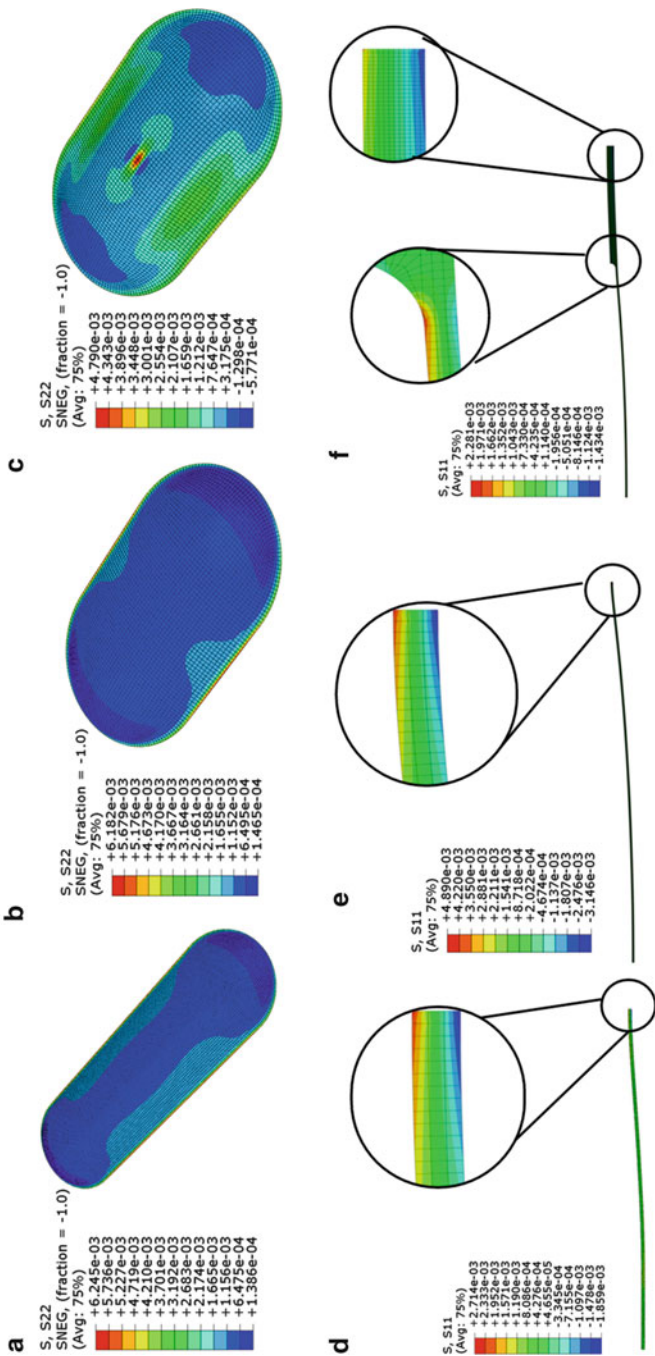


Fig. 6.11 Deflected shapes of the windows and the resulting stress distributions under 1 bar uniform pressure. *Top figure*: elongated membranes with lateral dimensions **(a)** 6×20 , **(b)** 6×10 , and **(c)** $3 \times 5 \mu\text{m}$. *Bottom figure*: axis symmetric models of circular windows in cross-section having **(d)** $3 \mu\text{m}$ and **(e, f)** $6 \mu\text{m}$ radii. The *small circles* in **(d-f)** indicate the transition from the thin electron transparent window to the thick SiN support. In **(f)**, this is two-step transition, firstly from the thin window to a thicker window as indicated in Fig. 6.12, and secondly from this window to the thick SiN support

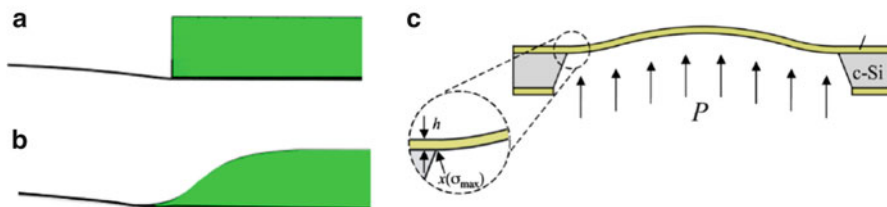


Fig. 6.12 Shapes of the models used for the calculations with (a) singular corners, (b) tapered corners, and (c) schematic of nanoscale bulge tests

Table 6.3 Summary of the simulated results compared to experimental failure probability

Applied load	1 MPa uniform pressure					
	15 nm thick elongated			15 nm thick circular		
Membrane type						
Lateral membrane dimensions (μm)	3×5	6×10	6×20	3	6	6
Variation in membrane thickness (nm)	–	–	–	–	–	15–60
Maximum out of plane deflection (nm)	105	215	256	66	170	115
Maximum tensile stress (10^{-3} GPa)	4.79	6.18	6.25	2.71	4.89	2.28
Failure probability	8 %	52 %	56 %	1 %	10 %	<1 %

The simulation results indicate that circular membranes have a much higher chance of survival under 10 bar pressure

Reliability and stiffness may be further enhanced by varying the thickness at the edges of the membrane

According to the simulations, the NR design with the elongated windows has an approximate 50 % chance of survival under 10 bar pressure. The results also suggest that the survival probability would increase to 99 % if the lateral window dimensions are reduced and if circular windows are taken with a varying cross-section as indicated in Table 6.3. Note that the probability of survival should be very high because failure of the membrane could result in a damaged electron source, of which a replacement costs 10,000 to 20,000 euro.

6.8.1.1 Experimental Mechanical Characterization Through Bulge Tests

It is quite common that the strength of materials shows significant deviations with changing size scales (Tsuchiya et al. 1998) and process parameters (Alan et al. 2006). Very little is known on the reliability of the use of bulk properties for simulations of the strength of ultra-thin structures. Therefore, we characterized the elastic properties and fracture strength statistics of Si-rich, low-stress SiN membranes with various thicknesses experimentally through nanoscale bulge tests (Paul and Gaspar 2008) (Fig. 6.12). To determine the mechanical properties and fracture strength statistics of SiN, 10, 16, and 1040 nm thick square and rectangular membranes with varying lateral dimensions ($0.5 \times 0.5 \text{ mm}^2$, $0.2 \times 2 \text{ mm}^2$, $0.9 \times 9 \text{ mm}^2$) were prepared with standard

fabrication techniques. Low-stress SiN films were deposited on an oxidized Si wafer. The wafer backsides were etched by a 33 % KOH solution, and the wafers were then immersed in a 7:1 buffered hydrofluoric acid (HF) solution releasing the membranes.

The wafers with released membranes were glued on supports that contained designated pressure feedthrough. The wafers were placed in the bulge test setup. This well-established method (Alan et al. 2012) consisted of measuring the out of plane deflection of the membranes under the influence of a uniform pressure. In the present setup, the out-of-plane deflections were monitored optically by an auto focus sensor, while pressure was applied from the KOH cavities on the wafer backside. After the dimensions of each sample were measured with an optical scan, the pressure was incremented in steps of 5 kPa. The deflected membrane profile was determined after each pressure step, and the maximum out of plane deflection at the center of the membrane was recorded. Repeating this procedure until fracture, the pressure–deflection curve and the maximum fracture load were determined for each of the tested structures. Further details of the experimental procedure can be found elsewhere (Paul and Gaspar 2008). The samples underwent deflections that were up to three orders of magnitude larger than the average film thickness and hence, the pressure–deflection curves were strongly dominated by the membrane effects. Here, the experimental data was analyzed using a model that considers the dominant membrane stresses, the rotation of the elastic supports, and the bending stresses that develop at the supporting edges. The Poisson’s ratio and Young’s modulus were then calculated by comparing the response of square and rectangular shaped structures based on standard membrane theory. The results are summarized in Table 6.4. The calculated elastic moduli, E , are smaller than the previously reported values (Paul and Gaspar 2008; Alan and Sarro 2008). Yet, they remain constant for different thicknesses. However, as the size scale changes from 1 μm down to 10 nm, the intrinsic stress in the films changes from tensile to compressive.

Finally, for each tested sample, the stress distribution corresponding to the fracture load was calculated. The maximum tensile stress value within each membrane was inferred as the fracture strength of the sample. Fracture strength probabilities from successive bulge tests are plotted in Fig. 6.13. As expected, there is a very strong dependence between sample size and strength. Strength increases fourfold from 2.9 to 13.5 GPa with decreasing sample thicknesses (a significant difference was not observed between the strength of 10 and 16 nm thick samples;

Table 6.4 Estimated material properties for SiN

Thickness h (nm)	Elastic modulus E (GPa)	Poisson’s ratio S	Intrinsic stress σ_0 (MPa)
10	142.9	0.3	−136
16	165.6	0.3	8.3
1040	162	0.3	94

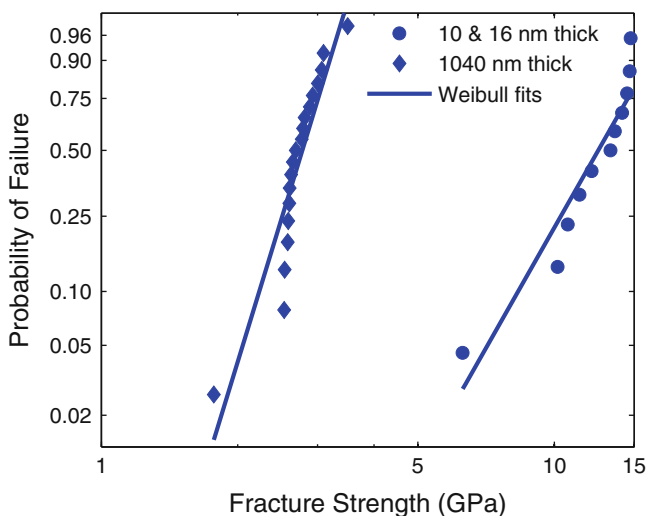


Fig. 6.13 Weibull strength distribution for rectangular membranes with different thicknesses. Strength increases from 2.9 to 13.5 GPa as membrane thickness is reduced (Alan et al. 2009)

hence, the data for both thicknesses were pooled). This size effect is generally attributed to the lower number of critical defects at smaller volumes.

6.8.2 Requirement 2: Allow Heating of Gas and Specimen with a High Accuracy in T

The MEMS heater has as big advantage that the power needed for the heating of the sample is small. In the design of the heater, this is achieved by realizing local heating inside or on top of the central part of a thin membrane. Because the heat conductance through the membrane to the supporting Si on the sides of the membrane is poor, one can easily obtain a temperature of 1000 °C in the center of the membrane, whereas the temperature of the Si hardly increases. We typically measure temperatures less than 40 °C for the Si chip for a heater temperature of 1000 °C. Note that the heat transfer to the Si chip depends on the distance from the heater to the Si and the thickness of the SiN. To reduce the heat transfer, one can increase the membrane size or reduce the thickness of the membrane, which indeed is an efficient way of heat transfer reduction, but increasing the size of the membrane width leads to more bulging of the membrane upon heating and a very substantial decrease in the membrane thickness can lead to more easy drum-like vibration of the membrane, which leads to loss of resolution when the sample is tilted.

Figure 6.14 shows a schematic presentation of the components in the heater chip and the holder that are relevant for the discussion on the drift properties of the total

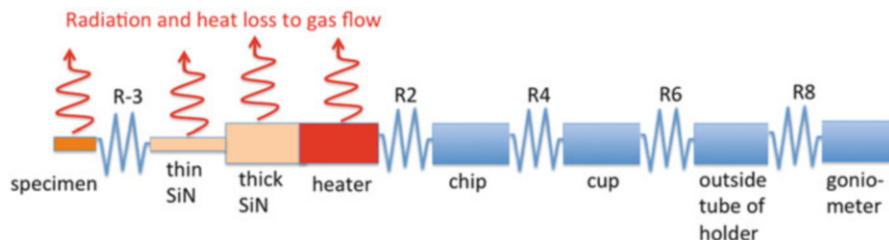


Fig. 6.14 Schematic representation of the various thermal resistors (R1–R8, where R3, R2, R4, R6, and R8 represent the connections between the various parts) that determine the heat transfer of the heater to the goniometer of the TEM. Note that the outer tube is connected to several parts of the goniometer with components that have their own thermal resistance and contacts with the final heat sink. Also the specimen itself, its contact with the support of the heater and the support-heater contact introduce thermal gradients and thus the real situation is more complicated than indicated here

system. Figure 6.14 depicts the various components as a series of thermal resistors. One can relatively easily determine the temperature of the heater by the resistance of the heater. This obviously requires a calibration, which for instance can be done on a local scale (e.g., 10 μm) using the Raman spectrum of Si (Hart et al. 1970) or carbon nanotubes (Huang et al. 1998). Once the heat distribution in the heater is characterized by local Raman spectroscopy, a pyrometer can be used to determine the temperature over a bigger area like 200 μm . The actual temperature of the specimen can be different from that of the heater because there are several thermal resistors between the sample and the heater (see Fig. 6.14). When the heater is in vacuum, a significant difference between heater and specimen only occurs if the temperature is well above 600 $^{\circ}\text{C}$. This is because radiation becomes important above this temperature. In this case, the sample temperature will be lower than the heater temperature to an extent that is determined by the radiation losses of the various components from heater to specimen and the heat resistances of these components. For instance, we noticed a difference in the evaporation speed of the Au particles on graphene suspended over an 8 μm hole in the SiN: the evaporation was significantly slower in the central part of the graphene sheet. At low temperatures, the radiation is relatively small and one can assume that the temperature of the sample is about equal to that of the heater even if the thermal resistance between the thin window and the sample is high because there is no energy loss.

When a gas is used (either in an ETEM or an NR), the situation is very different because the gas acts as a heat exchanger between the heater/sample and the surrounding area. Since the power to obtain the set temperature is steered by measuring the resistance of the heater, the effect of heat dissipation by the surrounding gas is fully taken into account. In Tables 6.5 and 6.6, two measurements are given, one for nitrogen and one for helium. The heat exchange of helium is much larger than that of nitrogen; the latter is comparable to that of oxygen and argon. The heat exchange of hydrogen is comparable to that of helium. For example, compared to heating in vacuum, the power required to heat the Pt wire

Table 6.5 Changes in power to microheater with applied pressure (as read from the gauge from the nitrogen bottle) in a nitrogen atmosphere

P (bar)	T ($^{\circ}\text{C}$)	R (Ω)	P (mW)	I (mA)
$\sim 10^{-3}$	37	169	0.102	0.77
$\sim 10^{-3}$	400	270	8.8	5.5
~ 0.1	400	270	20.1	8.60
~ 0.5	400	270	20.1	8.63
~ 1.0	400	270	20.2	8.65
~ 3.0	400	270	20.2	8.66

Table 6.6 Changes in power to microheater with applied pressure in a helium atmosphere as measured as the system was connected to a vacuum pump

P (mbar)	T ($^{\circ}\text{C}$)	R (Ω)	P (mW)	I (mA)
Helium				
10^{-5}	30	281	0.181	0.80
10^{-5}	400	387	8.60	4.72
10^{-4}	400	387	8.60	4.71
1.4×10^{-2}	400	387	8.69	4.75
10^{-1}	400	387	9.51	5.0
5×10^{-1}	400	387	11.2	5.4
1.0	400	387	13.4	5.9
1.5	400	387	15.5	6.3
2.0	400	387	16.8	6.6
5.0	400	387	22.6	7.4
10	400	387	27.1	8.1
20	400	387	32.4	8.9
40	400	387	35.3	9.6
50	400	387	36.6	9.8
100	400	387	38.5	10
250	400	387	39.9	10.1

to 400°C is about two times higher for 100 mbar nitrogen and four times higher for 100 mbar helium. A calibration based on a vacuum condition would lead to using an inaccurate required power to reach a certain temperature, i.e., the obtained temperature would be more than 100°C lower in both cases. This signifies the importance of a real temperature determination, for instance based on a resistance. In fact, a four-point resistance measurement can be realized by adding another resistor than the heater, but this would require two extra electrical contacts. It would also require some extra microfabrication steps in the cleanroom because the heater and the T measurement wires will be on top of each other and need to be separated by an isolating layer such as SiN.

Thus in order to have a reliable temperature in a gas environment, the temperature has to be controlled by a device component that allows for a temperature

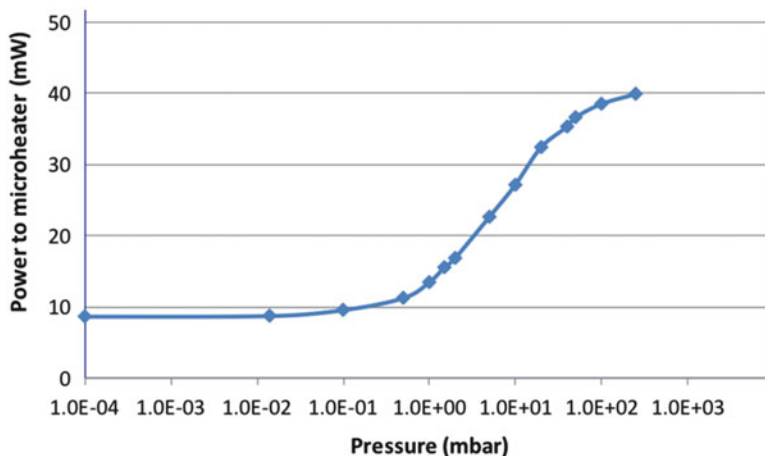


Fig. 6.15 Power needed for the microheater to maintain a temperature of 400 °C at different helium pressures

determination. This could be done for instance by constantly measuring the resistance of the heater (we are using this method) or by a Raman optical system. Note that the latter requires a dedicated TEM within-column space for the Raman optical microscope. We have used Raman for an ex situ calibration of the temperature distribution, for which we have built a dedicated measurement setup (Fig. 6.15).

Figure 6.16 shows simulations of the heat distributions in a vacuum environment of two types of heaters, a full spiral (left) and a flat center heater (right). In both cases, the thickness of the SiN is 400 nm. A disadvantage of the full spiral heater is that the central area with a diameter of about 100 μm with an equal temperature is not completely flat due to the presence of the Pt lines of about 150 nm thick. Due to this it is, for instance, difficult to place exfoliated graphene over the holes. The center part of the flat center heater is completely flat. Note that the central flat heater has a slightly lower temperature, which is due to radiation loss. An almost constant temperature for the flat center is seen for temperatures below 600 °C, where radiation losses are very small.

6.8.3 Requirement 3: Easy Loading of the Specimen

The samples to be studied with in situ TEM analysis are pieces of metals, ceramics, thin-films on substrates, or even soft biological materials. Over the years, several successful specimen preparation techniques for various kinds of materials have been developed for conventional TEM analysis. For conventional TEM studies, the most common specimen preparation techniques include electropolishing, ion-milling, grinding the specimen to extremely fine particles (<100 nm), and

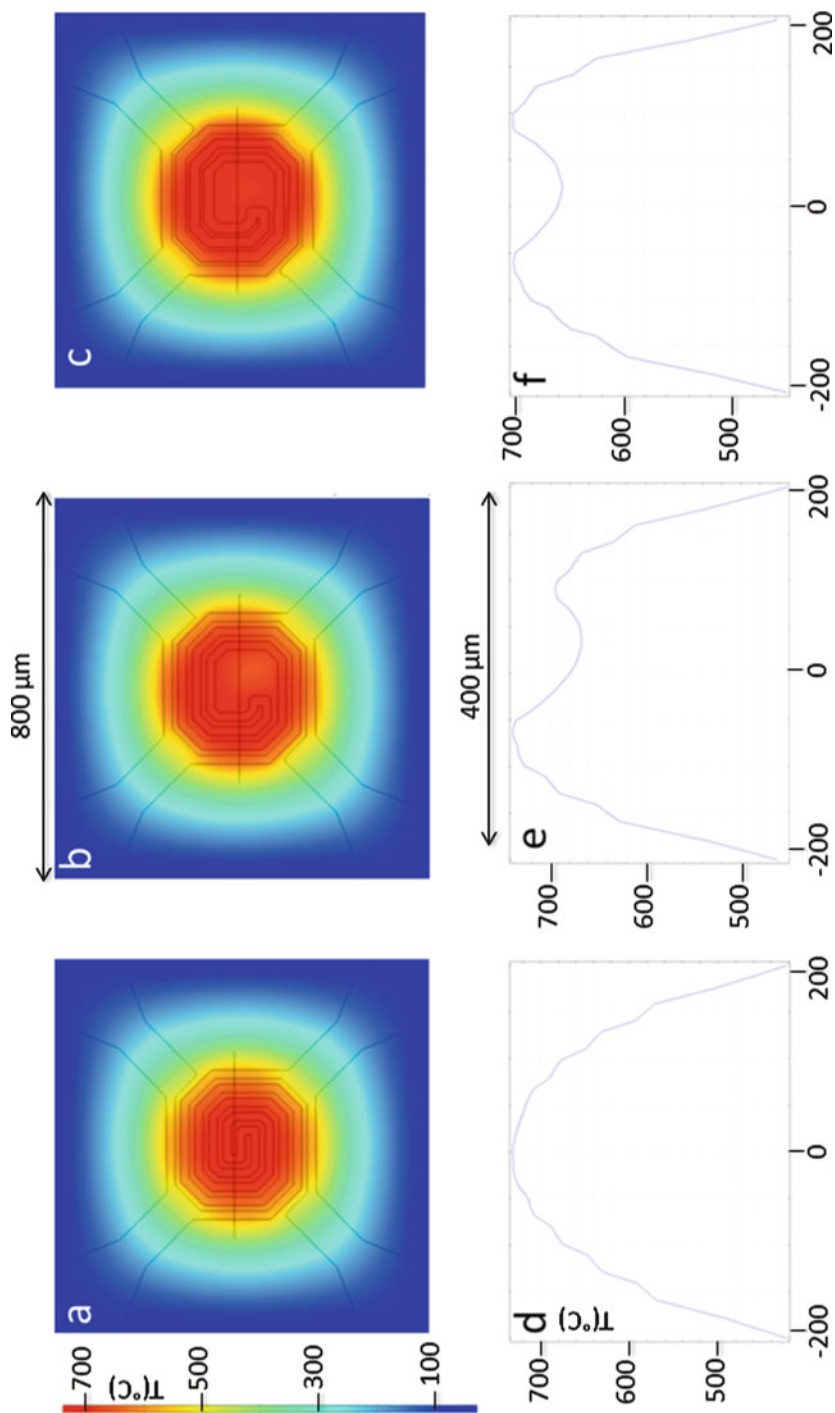


Fig. 6.16 Simulated temperature distribution across the membrane incorporating a Pt heating coil of different shapes. In (a), the spiral is continuous up to the center. In (b), a flat center area in the middle is present. On one side of the central flat area, four point lines are present and on the other side three point lines. Due to this, the temperature profile is asymmetric. In (c), the same asymmetry is number of lines of the heater is presented as in (b), but the width of the lines is adjusted such that a symmetric temperature distribution is obtained. The temperature profiles of the center $400\ \mu\text{m}$ of (a–c) are given in (d–f). With two types of heating coils, one with a continuous heating coil (a) and one with a flat center in the middle (b). (c, d) Represent line-scans of the temperature distribution in the NR along the horizontal axis through the center of the heating spiral. Similar results as to (a) are reported by Vendelbo et al. (2014), who included the presence of a CO gas

dispersing on standard TEM grids and specialized techniques like ultramicrotomy and focused ion beam (FIB). Almost all of these techniques can be adapted for in situ TEM studies using the NR provided the specimen is transferred successfully to one of the two chips (the chip at the bottom). Useful tips for loading the sample are given by DENSsolutions (<http://denssolutions.com/tips-tricks/sample-preparation/>). We have carried out an experiment on the dehydrogenation of Pd deposited on the top as well as the bottom membrane as a function of temperature and hydrogen pressure and observed that the temperature difference between top and bottom chip was less than 10 K. Nevertheless, it is best to put the sample on the chip half that contains the heater. Conventional TEM specimens are 3 mm circular discs that fit in standard specimen holders. However, owing to the limited size of the microheater and the electron transparent windows the sample size in an NR is more limited. Since one wants to keep the distance between the two membranes small, the sample should also be thin over the whole lateral shape (e.g., less than 2 μm). In addition, really thin sample areas are required over some of the electron transparent windows (typically ~ 5 to 20 μm in diameter). Of course, the thin part of the specimen should precisely be placed on such a window.

Ceramic TEM specimens are prepared by just crushing a bulk material and putting them in suspension. Nanoparticle suspensions or suspensions of biological specimens are best transferred by sonicating the suspension for sufficient amount of time and drop casting a sample. Because the densities of these suspensions are usually high enough to cover most of the TEM windows, there is enough material to carry out in situ TEM studies.

Bulk metallic specimens and thin-films over substrates for which cross-section specimens are required, specimen preparation using FIB works best. An added advantage of using an FIB is that very specific areas of interest can be selected. Examples are cross-section samples across an interface, specimens from a special phase, and specimens corresponding to a specific crystallographic orientation (Fig. 6.17). Such specimens are typically of the size $\sim 15 \mu\text{m} \times 5 \mu\text{m}$ with thicknesses $\leq 100 \text{ nm}$.

Specimens can be transferred to the TEM windows of an NR very precisely by using an in situ micromanipulator available on most modern FIBs or by using the conventional ex situ micromanipulator employing a glass capillary with a sharp tip. An example of FIB cross-sectional preparation across a grain boundary in an aluminum alloy and its ex situ transfer using a glass micro capillary is shown in Fig. 6.17c–e. If there are specific areas of interest in conventional 3 mm disc specimens, these areas can be cut precisely using the FIB and transferred to the bottom chip. Upon successful transfer, the specimen is ready for either in situ heat-treatment studies using a heating-holder compatible with this bottom chip or, for in situ environmental TEM studies when the bottom chip is coupled to a top chip to make an NR as shown in Fig. 6.18.

The bottom and the top chips are first positioned facing each other in a custom-made alignment tool as shown in Fig. 6.7. The procedure of alignment starts with coarsely positioning the top chip (facing downwards) such that the large SiN windows in both the top and bottom chip coincide with each other. The alignment

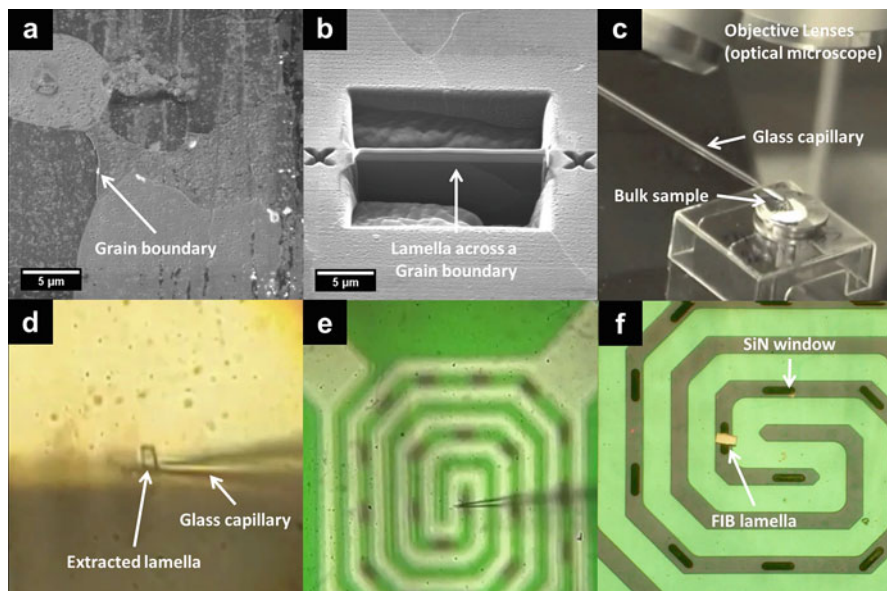


Fig. 6.17 (a) FIB-SEM image showing grain boundaries in an aluminum specimen. (b) FIB cross-sectional lamella prepared across grain boundary shown in (a); the lamella at this stage is cut and finally thinned to thickness <100 nm and released to stand freely in the cavity. (c) Photograph showing glass capillary controlled by a hydraulic micromanipulator. (d) Optical micrograph focused on extracted FIB lamella from a cavity as shown in (b). (e) Optical micrograph focused on glass capillary positioned precisely over a TEM window; the hydraulic micromanipulator allows positioning the lamella with an accuracy of ~ 2 μm . (f) FIB lamella deposited over a thin SiN window, ready for imaging either for in situ heating experiments, or for assembling an NR

tool consists of micrometer screws connected to metal plates which displace the top chip with ~ 1 μm step size. The alignment tool has the capability to precisely displace the top chip only in the XY -plane. In order to avoid any displacements in the Z -direction, the top chip is restricted to just horizontal movement by fixing the lid. Once the window(s) of the top and the bottom chip coincide, the top chip is moved down in the Z -direction by gently screwing down the lid. While fastening the top chip, one has to be very careful not to damage the top chip by any excessive torque. An indication of the right channel height for in situ TEM experiments is that both the top and the bottom chip are visible in the same focal plane in the optical microscope.

The alignment tool described here requires the NR to be glued either by an epoxy-based glue, super glue, or water glass. This principle of aligning the top and the bottom chips together has been extended further to avoid gluing altogether by including an O-ring in between the chips by creating a groove in the top chip. For this, the alignment tool has been adapted to allow either a retractable tip or a TEM holder with gas-flow channel. In these cases, the top chip is held in position after alignment by the lid. The O-ring in between the chips helps to maintain the NR leak-tight to allow live imaging inside the TEM.

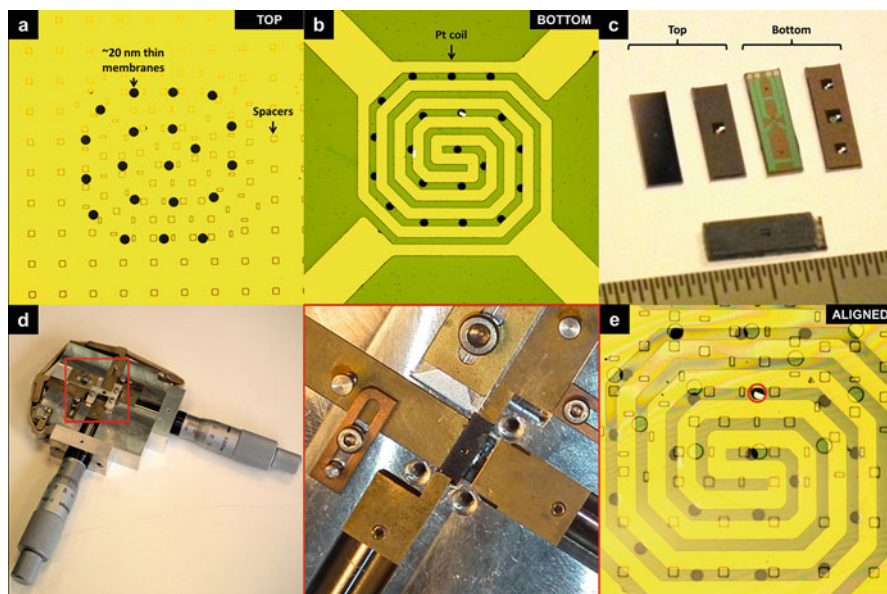


Fig. 6.18 Optical micrographs showing the large SiN windows of (a) the *top* chip and (b) *bottom* chip. These windows are at the *center* of the chips shown in (c). The *bottom* chip is placed facing upwards in the alignment tool shown in figure (d) while the *top* chip is placed facing downwards. Zoomed image of the area bounded by *red box* at the *center* of the alignment tool shows the metal plates connected to micrometer screws which displace the *top* chip with displacements as small as $\sim 1 \mu\text{m}$. The lid is placed over the chip assembly and tightened enough to allow displacement only in the *XY*-plane. After the window(s) in the *top* and the *bottom* chip are aligned as shown in (e), the NR is ready for gluing to be used either in a static gas system or a flow-gas system

6.8.4 Requirement 4: Allow a Controllable Gas

Ultimately, one would like to control the gas pressure and the composition to the extent that both can be changed instantaneously. This is, however, not possible due to the geometry of the NR and the geometry of the holder. The NR has very narrow channels creating barriers for the fast gas flow, needed for a rapid gas exchange. Thus the small size of the NR, giving on the one hand the advantage of fast temperature changes without experiment-limiting specimen drift, has on the other hand the disadvantage of slow gas exchange. Also, the NR is only hot in the center of the two membranes, and the rest of the NR is at about room temperature. Thus, some of the reaction products could be deposited on the cold part of the NR. Furthermore, the diameter of the TEM holder does not allow for electrically controlled valves close to the NR. Therefore, the gas tubes of the holder have to be pumped to exchange the gas.

If one needs only a fixed gas pressure, one could use a static gas holder for which the exchangeable tip can be extended with a pressure meter for instance. This requires extra electrical wires at the outside of the holder, making the holder

more complicated. If one needs a gas flow or a change of the gas composition, a flowing gas holder is required. As mentioned in Table 6.2, the static gas and flowing gas holders have their own advantages and disadvantages.

6.8.5 Requirement 5: Compatibility with Normal TEM Operation

One of the big advantages of an NR over an ETEM is that the experiments can be done in any TEM, provided that the holder is completely compatible with the normal operation of a standard TEM sample holder. This is fairly easy to realize. Note that with this approach also low-end TEMs can be used, which are actually sufficient for quite some experiments. With the possibility to use also low-end TEMs, in situ TEM is also attainable for relatively less equipped research groups. Note in this respect that for an LaB₆ type of electron source the restrictions on airtightness of the NR and the holder are less stringent. This is because in the case of a collapse of the NR, damage to the gun is less severe and replacing the gun is much less costly and time consuming than for an FEG. We have never had a problem with a collapse of the NRs, even in high-risk experiments in which we explored the maximum pressure or temperature allowed, for which we typically used our LaB₆-operated TEM.

The gas holder can be made completely compatible with a standard goniometer, such that the in situ experiments are not hampering the normal use of the microscope in any way.

6.8.6 Requirement 6: The NR Should Be Easy to Use and Made as Disposable

The challenges involved in in situ TEM experiments at relatively high gas pressures require sophisticated MEMS fabrication to obtain reliable miniaturization. The sample clamping and preparation need to occur at a very high control, which typically requires about 40–100 cleanroom process steps. Evidently, these challenges become more difficult when one wants to combine several external stimuli such as an electrical measurement in a gas environment. If more stimuli are added, a further miniaturization has to be realized, given the limited available space in the electron microscopes.

6.8.6.1 The Cleanroom Process for the Sandwiched NR

The design of the sandwiched NR consists of two different chips which are an MEMS-based heater chip (bottom) and O-ring chip with grooves (top). The

MEMS-based heaters that are presently used in the NRs are the same as those for in situ heating TEM studies. These heaters have been shown to be very efficient in TEM studies, such as morphological transformation of gold nanoparticles (Young et al. 2010), sculpting of graphene (Song et al. 2011), thermal stability, and degradation of nanoparticles (Yalcin et al. 2014). The heaters have platinum (Pt) as the heat-conducting material, which is embedded in a ~ 400 nm thick SiN membrane with $6 \mu\text{m}$ wide viewing windows of ~ 20 nm thick SiN. Since the embedding requires two SiN deposition steps, Pt has to be stable in the gases used in the second SiN deposition. In the case of an NR, embedding of the Pt by SiN is essential to prevent that Pt is reacting with the experimental gas. Our MEMS heater contains four electrical connections that allow for temperature determination and heating. The other chip (also called top chip) has a groove depth of $\sim 300 \mu\text{m}$ for the O-ring. The top chip consists of a ~ 500 nm thick SiN membrane with $12 \mu\text{m}$ wide viewing windows of ~ 20 nm thick SiN. MEMS-based heaters and top chips can withstand at least 1 bar pressure.

In Fig. 6.19, the fabrication steps are shown for bottom and top chips. The steps include low-pressure chemical vapor deposition (LPCVD) of SiN, plasma-enhanced chemical vapor deposition (PECVD) of SiO_2 , lithographic definition, dry and wet etching, dicing, and cleaning. Both Si wafers have an initial thickness of $500 \mu\text{m}$. The initial step to fabricate a heater is LPCVD of 200 nm thick SiN that acts as an isolation layer between Pt and Si. The platinum layer is embedded in ~ 400 nm thick SiN layer in total. Subsequently, by optical lithography the viewing windows with a diameter of $6 \mu\text{m}$ are patterned onto SiN layer by anisotropic plasma etching based on AR and CHF_3 . The last LPCVD step is performed to obtain 20 nm thick SiN electron transparent viewing windows. The silicon substrate is etched by KOH to get SiN membrane devices. The final steps are dicing the wafer and cleaning which leads to carbon-free, non-contaminated high quality chips.

Similar to heater chips, the production of the top chips is started from a $500 \mu\text{m}$ bare silicon wafer. PECVD of SiO_2 is used as a mask layer, and the $\sim 300 \mu\text{m}$ depth grooves are patterned and transferred to silicon layer by SF_6 -based dry etching. The mask layer SiO_2 is removed by selectively wet chemical etching with buffered HF. LPCVD SiN is performed to get membrane ~ 500 nm. The viewing windows with a diameter of $12 \mu\text{m}$ are patterned and transferred to SiN layer. The size of these windows is bigger than the size of the windows in the heater to increase the alignment tolerance. The thin SiN deposition is performed, and silicon is etched by KOH from the back side to create a free standing SiN membrane. The size of the top chips is slightly smaller than the heaters to have space for electrical contact pads, see Fig. 6.2.

6.8.6.2 The Cleanroom Process of the One-Chip NR

The cleanroom process of fabricating the one chip NR is sketched in Fig. 6.20 (Creemer et al. 2011). The process roughly consists of the following steps: (1) Growth of wet thermal SiO_2 on a 100 mm Si wafer ($0.2 \mu\text{m}$); (2) Deposition of low-stress SiN_x ($0.7 \mu\text{m}$); (3) Photolithography and wet etching holes for

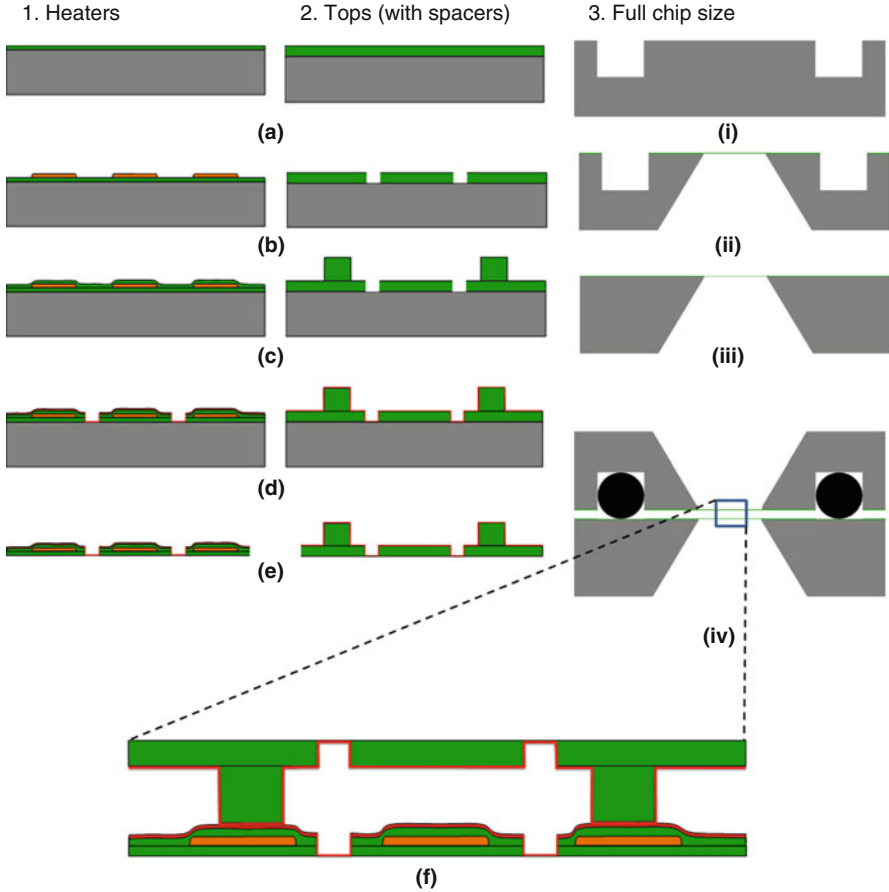


Fig. 6.19 Schematic cross-section of fabrication steps for heaters (1) and top chips (2) are demonstrated. (3) Shows the full size chip for heaters and tops for better understanding of sizes. (1a) and (2a) are deposition steps of SiN. (1b) is obtaining the Pt/Ta after deposition and etching, while (2b) is opening the electron transparent windows with optical lithography and dry etch of SiN. (1c, 2c) are LPCVD of SiN as a cladding layer for heater and spacer for *O-ring* tops, (1d, 2d) after lithography of viewing windows and deposition of ~20 nm thick LPCVD SiN. (1e, 2e) Are the final step of fabrication which are after back side lithography and wet etching of silicon by KOH. (3i) is after opening the *O-ring* grooves and (3ii) is after KOH etching of Si. (3iii) Shows the heater chip after KOH, and (3iv) is the full size of chips when they are mounted together including the *O-ring* rubber with the enlarged view in (f)

electron transparent windows; (4) LPCVD of Tetraethyl orthosilicate (TEOS) as a sacrificial layer (1.0 μm); (5) Patterning of TEOS for pillars by using buffered HF (BHF); (6) Deposition of top SiN_x (0.5 μm) and plasma etching to create access holes to remove the TEOS in BHF; (7) Inside coating with TEOS and 15 nm SiN; (8) Plugging the access holes with SiN; (9) Creation of the Pt heater; (10) Local KOH etching of the mono Si to expose the electron transparent windows.

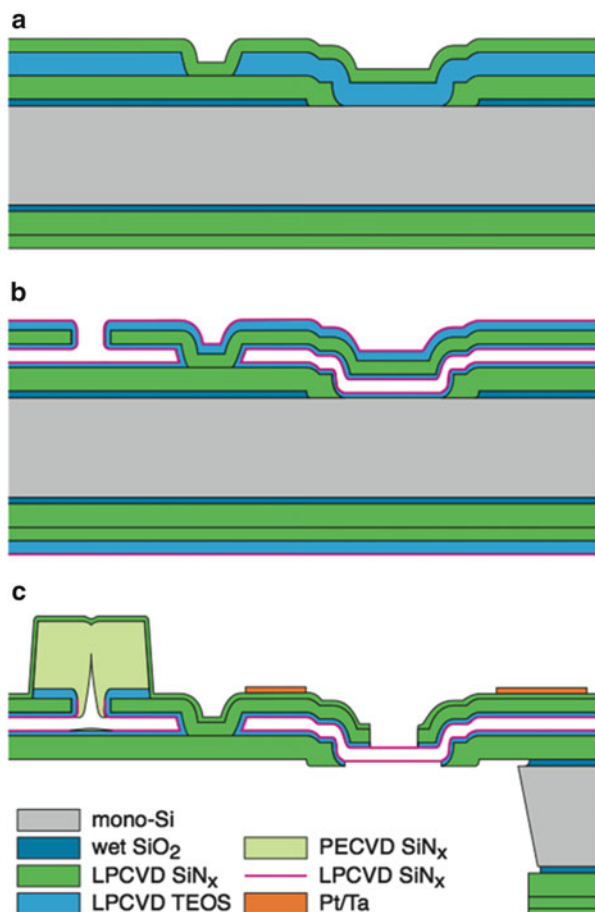


Fig. 6.20 Schematic cross-section of the NR, in different stages of the fabrication (Creemer et al. 2011). **(a)** Initial depositions of wet thermal SiO₂ and low-stress SiN_x, followed by photolithography and wet etching holes for electron transparent windows, and deposition of LPCVD TEOS sacrificial layer. **(b)** Sacrificial etching and internal coating of the channel with the window material. **(c)** Final thin-film structure: plugged channel, released windows. *Fabrication steps:* Growth of wet thermal SiO₂ on a 100 mm Si wafer (0.2 μm). Deposition of low-stress SiN_x (0.7 μm). Photolithography and wet etching holes for lower electron transparent windows. Deposition of LPCVD TEOS as sacrificial layer (1.0 μm). Patterning TEOS for pillars using buffered HF (BHF). Deposition of top SiN_x (0.5 μm) and plasma etching to create access holes to remove the TEOS in BHF. Inside coating with TEOS and 15 nm SiN_x. Plugging the access holes with SiN_x. Creation of Pt heater. Local KOH etching of the mono Si to expose the electron transparent windows

The important concept is the introduction of a sacrificial TEOS layer that can be removed later in the process, followed by (a) the internal deposition of again an LPCVD TEOS layer as an etch stop for later steps, and (b) the LPCVD SiN_x electron transparent 15 nm layer (exposed later by a KOH etch of the

monocrystalline Si substrate). The access holes to remove the sacrificial layer are “plugged” by a PECVD SiN local layer sealed with another PVCVD SiN layer. The resistive heater is made by evaporation of Pt (0.2 μm) on top of an adhesion layer of Ta (15 nm) with the aid of a lift-off process. The final steps are the release of the electron transparent windows using buffered HF etching. The inlets and outlets of the channel are created by plasma etching using a shadow mask.

6.8.7 Requirement 7: The Carbon Contamination Should Be Negligibly Small

Since the characterization of a material under a gas atmosphere requires that the surface is very clean, the formation of C-contamination has to be prevented during the in situ TEM experiments. If available, a reliable method to remove any carbon is required. Keeping the sample free from C-contamination usually requires the absence of hydrocarbons, whereby the presence of water accelerates the formation of C-contamination. Note that the electron beam is an extremely efficient hydrocarbon “detector” because the electron beam can crack the hydrocarbon very efficiently to C. The presence of water plays an important role because it strongly effects the surface diffusion of hydrocarbons and probably plays a role in the cracking process as well. For instance, heating a sample in vacuum at 300 °C for a few minutes allows for subsequent C-deposition-free experiments at room temperature (see Fig. 6.21). Alternatively, cooling of the NR to, e.g., -60 °C while heating of the membrane to, e.g., 400 °C will allow trapping of water and hydrocarbon molecules outside the reaction area, thereby strongly reducing the formation of C-contamination as we have verified experimentally.

In Fig. 6.21, the deposition of C can be observed well, if one defocuses. In this case, a thick contamination was deposited by a beam roughly of the size of the contamination. Note that if a larger beam size is used, most of the contamination is deposited as a ring at the edges of the beam. If the C-deposition is much smaller than that shown in Fig. 6.21a, it can be difficult to verify the absence of any C-deposition. When a hole is available, C-deposition can be observed by growth of the edge as explained in Fig. 6.21b. When a hole like the one in Fig. 6.21b is not available and the C-deposition is small, we use a small spot size of, e.g., 5 nm and keep the beam for about 10 min at the same position (so no drift should be present) with the sample at about zero focus (to be sure that the actual beam on the sample is indeed small). Note that the beam should not be so intense that a hole is drilled in the electron transparent window as in Fig. 6.21b. Next at high under focus or over focus we check whether there is a local intensity change. If there is a hole as in Fig. 6.21b, we put the beam on the edge of the hole (as the yellow dot in the inset of Fig. 6.21b and keep it there, e.g., 10 min. In the case of C contamination, the edge will “grow” along the edge of the beam. If the growth is relatively fast, one can see it if the recording is done in movie mode.

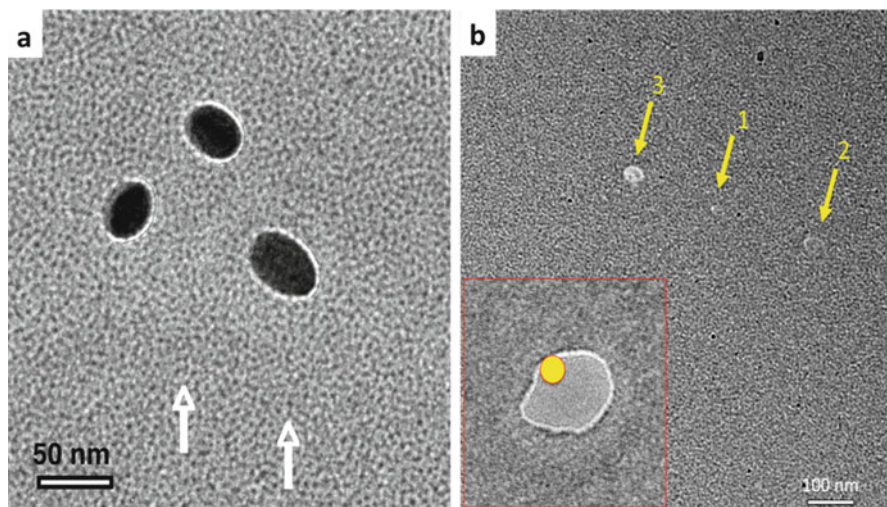


Fig. 6.21 (a) Three C-contamination dots deliberately created on a C film using a dirty C film on a MEMS heater, by focusing the electron beam on these three areas for 2 min. Next, the sample was heated at 200 °C for 2 min. Subsequent focusing of the electron beam at the areas indicated by the *white arrows* for several minutes did not lead to any visual contamination. Note that a strong defocus was used to image the C-contamination dots. (b) shows that a very intense fully focused electron beam can remove SiN finally resulting in a hole in the SiN membrane. The beam was positioned at the locations indicated by the *arrows 1, 2, and 3* for 1, 2, and 5 min. At *arrow 3* a hole is present. This hole can be used for a precise determination of the absence of C-contamination, by putting a beam with a relatively low intensity such that no SiN is removed at the edge of the hole as the *yellow spot* in the *inset* in (b). In case of any C-contamination, one can see the growth of material at the edge real time

6.8.8 Requirement 8: The Electron Transparent Membranes Should Be Uniform in Thickness and Amorphous

Preferably, one would like to have no effect of the presence of the two membranes, but this is not possible of course. Typically, one wants to image the sample relatively close to zero focus. In this condition, one of the two membranes will also be close to zero focus, but the other one will not be and the modification of the electron wave by this membrane can be significant. This can be seen in Fig. 6.22, where two samples are shown at zero focus and 10 μm focus. Clearly, the effect of the membrane is much less at zero focus. Furthermore, it is clear from Fig. 6.22 that thickness variations (in the form of local bumps) can have a strong effect on the image. Therefore, the interpretation of a sample between one or two windows with thickness variations will be less easy. Therefore, we have put quite some effort in making uniform windows, which are as thin as possible. During the deposition of the thick SiN for the electron transparent windows, we add an Si test wafer, which can be tested for roughness using STM. Typically, we get a roughness of 0.4 nm RMS. Note that even when one has perfectly uniformly thick electron transparent

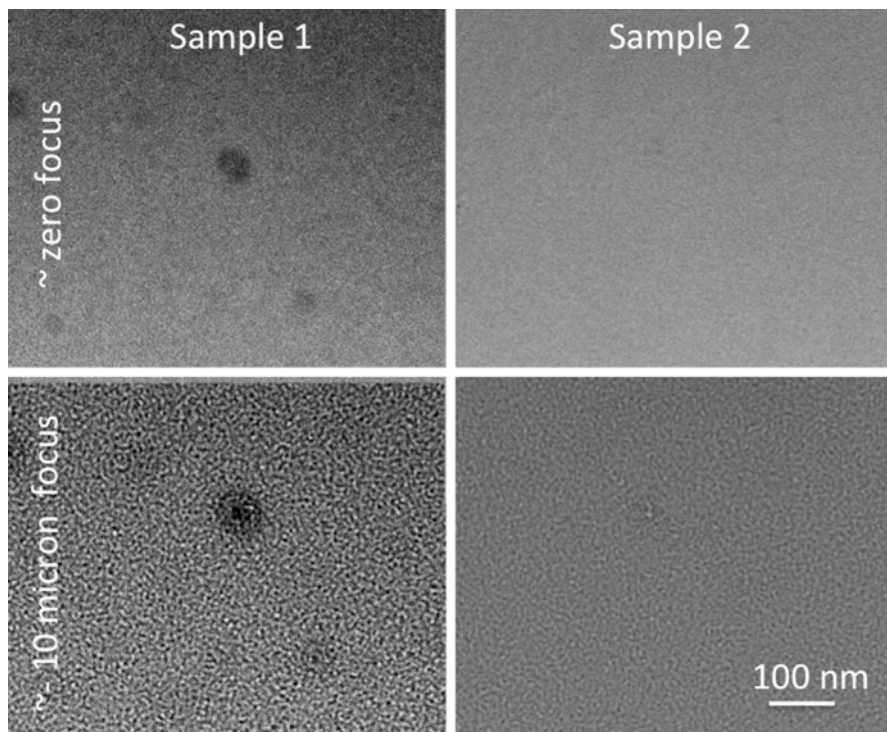


Fig. 6.22 Example of two electron transparent ~ 20 nm thick SiN windows at zero focus and a focus of about $-10 \mu\text{m}$. In the *left* example, SiN-like particles are present of different sizes. In the *right*, hardly any particle can be observed. Note that such particles are much better visible if the imaging is done at high under or over focus

windows, the relative positions of areas of interest can affect the measurement. For example, when both membranes are covered with particles of the sample to be studied, particles on one membrane will strongly hamper the study of particles on the other membrane if their projections partly coincide in one or more of the required viewing directions.

6.8.9 Requirement 9: The Length of the Gas (or Liquid) Column Should Be Small (Matching the Required Resolution)

We have done experiments with thin SiN electron transparent windows to determine the minimum required thickness to maintain a 1 bar pressure difference over the window without breakdown. We have noticed a significant failure rate ($>10\%$ of 10 chips with each 16 electron transparent windows) when the windows were 10 nm or

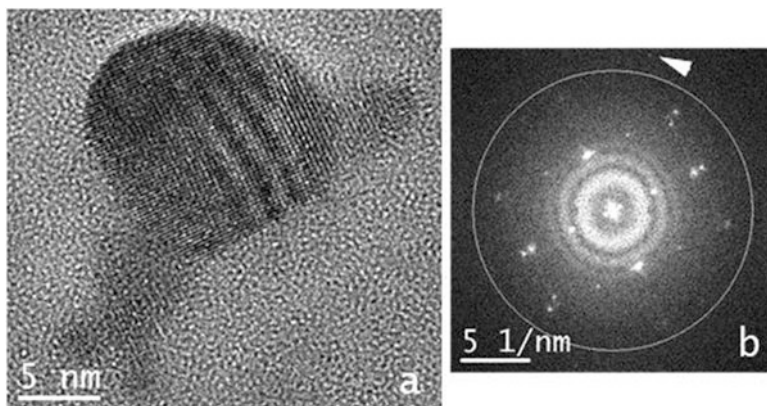


Fig. 6.23 (a) PdO_x nanoparticles in O₂ with pressure of 0.65 bar at 500 °C. (b) FFT of image (a), the white circle is 1 Å. The *triangle* indicates a diffraction spot with a d-spacing of 0.88 Å. Note that the rings in the FFT are from the window not carrying the particle

thinner. Note that such a test will depend strongly on the quality of the deposited SiN. A thickness of 20 nm might be required for other SiN depositions to obtain no failure.

Assuming the thickness of the SiN windows is 15 nm, the total thickness of SiN is thus 30 nm. Taking as rule of thumb that the density of a gas at 1 bar is 1000 times smaller than the solid (of the same composition), a gas column of 20 μm of O₂ gas at 1 bar will be equal to 20 nm of solid O₂. The latter has a lower scattering potential than the two 10 nm thick SiN windows. Under these conditions, a good resolution can still be achieved as it can be seen in Fig. 6.23. This back-on-the-envelope estimation also shows that a large reduction of the gas column is not very useful, if the thickness of the SiN windows is not significantly reduced.

One could use thinner SiN membranes if the failure rate is reduced or by using a lower pressure in the NR. Note however, that normally the holder is first in air and thus the pressure on the outside of the NR is 1 bar and once inside the holder this pressure drops quickly to 0 bar. Starting for instance with a pressure of 0.1 bar inside the NR, one has a pressure difference of 0.9 bar. Only if the pressure inside the NR is kept the same as outside the NR by a shunt between the inside of the NR and the vacuum of the microscope, one can use electron transparent windows that do not withstand a 1 bar pressure difference.

6.8.10 Requirement 10: The Resolution Should Preferably Be the Same as that of a Standard Holder

If an HRTEM that allows 1 Å resolution is used for the NR experiments and this resolution is lost because of the NR-holder-HREM ensemble, the reason for the resolution loss can be: the thickness of the SiN membranes, the thickness of the gas

column, specimen drift, mechanical instability of the holder/NR ensemble, charging and other electrical instabilities, and/or the holder–goniometer interface. The specimen drift is discussed in more detail below. Our experimental results in getting 1 Å resolution show that all causes for resolution loss can be overcome.

In many cases, one is interested in experiments for which a relatively large field of view is needed. For instance, if the front of the oxidation of Pd to PdO moves fast and over a big area, one gets much more information from an overview movie with a relatively low resolution than a low field of view HREM movie.

Given the contradictory requirements of a high field of view and sometimes very detailed imaging, the best option is a combination of two detectors, whereby the first detector has a hole behind which at some depth a second camera is placed. If both cameras have $4k \times 4k$ pixels and the first one has an effective pixel size of 0.1 nm/pixel and the second one a pixel size of 0.02 nm, the problem is how to display this in an efficient manner given the nature of the human eye. The display should be such that: both images are displayed on the same monitor or an array of monitors; whereby the image of the second detector is shown in the center, and the first detector is displayed around this central area with the same magnification as the second detector and thus with 5×5 pixels in the display for each pixel of this camera. In this display mode, one can use the human eye, which is fine-tuned for focusing on the center with high resolution and still be able to detect movements and rapid changes in the periphery.

6.8.11 Requirement 11: The drift Should Be Small Enough to Record High-Resolution Images

We typically set our goal for the drift to be less than 3 nm/min. This allows 1 Å resolution imaging with an exposure time of 0.5 s, which we consider as a standard recording time. Such drifts are well obtainable as shown in the example in Fig. 6.23. In the case of imaging of changes, one prefers to obtain as many images as possible, and in such case exposure times of 0.5 s are rather long. Therefore, the possibility to record high-resolution images is not limited by the holder or NR.

6.9 Electron Beam Effects

Well-known artifacts of the electron beam during TEM experiments were evaluated for example by Egerton et al. (2004), also see Banhart (1999). Major artifacts are electrostatic charging due to bad electrical connection between the specimen and the holder, structural damage, and sputtering of the sample as the result of knock-on damage (elastic scattering of electrons) and radiolysis (inelastic scattering of electrons), specimen heating caused by inelastic scattering of the incoming

electrons by the specimen, and deposition of material on the specimen and support, i.e., carbon deposition due to hydrocarbons on and around the specimen. These artifacts depend to a large degree on the electron beam energy and intensity. For example, sputtering of the specimen can be neglected at 100 kV or lower, but will occur at 200 kV for light elements like carbon or silicon.

Aside the normal electron beam artifacts, important artifacts encountered in an NR are contamination and damage of the electron transparent windows or the specimen by the electron beam. Contamination of the specimen and the SiN windows caused by cracking of hydrocarbons inside or outside the NR by the electron beam is an important issue as described above: the presence of water molecules in the system has a major impact on the contamination of the sample caused by the cracking of hydrocarbons by the electron beam on the sample surface, see the experiments described in Fig. 6.21. Sputtering of the electron transparent SiN windows must be avoided obviously, since a hole drilled by an intense electron beam will create a leaky NR. In Fig. 6.21, an example of a hole drilled with an electron beam is visible. Typical electron doses used for hole drilling were reported as $\sim 10^8$ e/nm²s (5 nm beam diameter, 200 kV) in a 40 nm thick SiN/SiO₂ window (Wu et al. 2005), and $\sim 1 \times 10^8$ Am⁻² in 10 nm thick SiO₂ windows (using a few nm beam diameter at 300 kV) (Storm et al. 2003).

Dose rates should be kept at a low value to avoid a visible influence of the electron beam on the sample under investigation itself. Vendelbo et al. (2014) found that at dose rates of 10,000 e/nm²s (300 kV) and above, the investigated Pt nanoparticles in a O₂/CO gas-loaded NR are displaced in the projected image plane. In (de)hydrogenation experiments up to 4.5 bar H₂ in an NR (Yokosawa et al. 2012), an electron dose up to 1000 e/nm²s (300 kV) did not influence the phase transition temperature.

6.10 Examples of Experiments

In this section, a few case studies will be presented to show the application of different NRs in in situ TEM experiments for understanding processes involving gas–matter interactions.

6.10.1 In Situ TEM on (de)Hydrogenation of Pd at 0.5–4.5 Bar H Pressure and 20–400 °C Using a Composite Flowing Gas NR

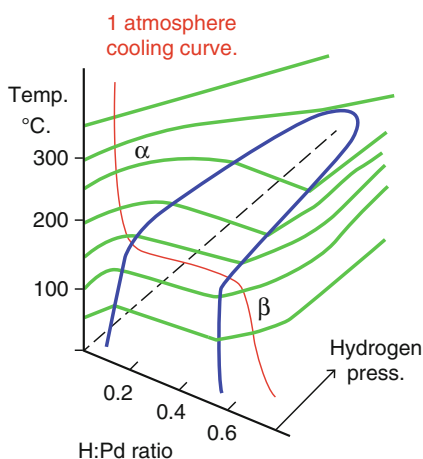
The composite NR was used (Yokosawa et al. 2012) to study the (de)hydrogenation of Pd crystals at hydrogen pressures up to 4.5 bar. An LaB₆ electron source in a Philips CM30T TEM was used for imaging. A dedicated gas handling system with

tubing to the NR TEM holder was used to regulate the hydrogen pressures ranging from 0 to 10 bar. Image plates were used for recording images and diffraction patterns. Also movies of the dynamic diffraction patterns were recorded during phase transitions using a Gatan Fiber-Optic Coupled Camera (25 fps).

A Pd thin-film was sputtered on the SiN of the bottom chip with the heater spiral, including the electron transparent windows. Heating to ~ 400 °C transformed the randomly oriented Pd crystals into closed Pd islands, which were 50–1000 nm wide and 15 nm thick. The distance between the 300 μm wide SiN windows was limited to 3 μm (no bulging) at vacuum (short cut to vacuum of TEM) and to 19 μm at 3.2 bar hydrogen gas, as measured by focusing at the bottom and top electron transparent window edges. This was less than when 1000 μm (in which case the bulging was about 36 μm) wide windows were used. However, with the smaller membrane diameter the temperature gradient is larger because the neighboring Si support acts as a heat sink. This temperature gradient and the indirect heating of the Pd crystals through the gas give some uncertainty about the temperature at the crystal. However, the observed α to β phase transition temperatures (see Fig. 6.24) correspond to the bulk measurements reported (Qian and Northwood 1988).

The phase transitions due to changes in temperature or pressure were visualized by using the differences in lattice parameters of the phases. Movies of selected area diffraction patterns were recorded. In Fig. 6.25, a series of patterns is shown after a sudden temperature drop from 140 °C to room temperature in a 0.8 bar H_2 atm. The lattice expansion caused by the hydrogen absorption results in a 3 % shrinkage of the (022) reflections in the patterns during the few seconds for the transformation to occur. Both the Pd and the PdH reflection are observed for single Pd crystal transforms during 1 or 2 s. This shows that the transformation occurs gradually and that the crystal orientation of the PdH is the same as the original Pd crystal. This was also observed from careful dark-field imaging during the transition by aligning the objective aperture at the position of the PdH reflection, thereby just omitting the closely positioned Pd reflection: it showed a gradual intensity increase from a crystal upon hydrogen absorption during 4 s.

Fig. 6.24 Schematic Pd-H phase diagram. The H poor α -phase is fcc structured with lattice parameter 3.89 Å as pure Pd. The NaCl structured β -phase has lattice parameter 4.03 Å



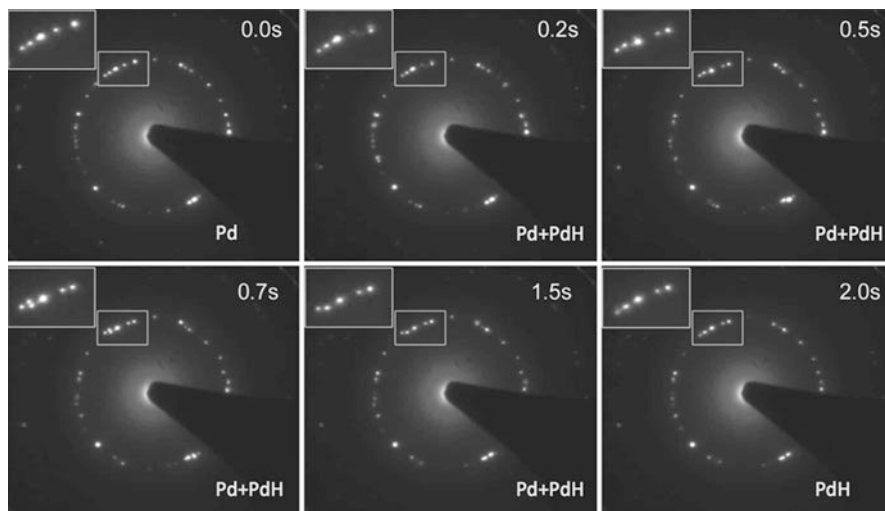


Fig. 6.25 Selected area diffraction patterns of a number of Pd particles with different orientations, after decreasing T from 140 °C to RT. The lattice expansion caused by the hydrogen absorption causes a 3 % shrinkage of the (022) reflections. At 0.7 s after the decrease in T , a “split” reflection is seen: this indicates a transition was going on from Pd to PdH during the recording of this pattern. The transformations of different crystals do not occur all at the same time

By changing the temperature in the NR gradually, a transition temperature can be found from the dynamic diffraction pattern. This is a more direct method than changing the pressure because a change in temperature is much faster. The transformation was shown to be reversible, but a hysteresis was observed between the α to β and β to α phase transition temperatures of 15 °C at 0.5 bar H_2 and 7 °C at 4.5 bar H_2 . The pressure dependence of the transition temperature and the hysteresis is shown in Fig. 6.26. It is similar to the hysteresis found in bulk materials, showing the reliability of the in situ method. The in situ method presented by Yokosawa et al. (Yokosawa et al. 2012), however, showed differences in the transition behavior of individual Pd(H) particles: some particles were shown to transform consistently faster than others. Thus, the use of NRs for in situ TEM provides a tool to investigate (de)hydrogenation properties on a local scale.

6.10.2 Oscillatory CO Oxidation Catalyzed by Pt Nanoparticles Using Time-Resolved High-Resolution Transmission Electron Microscopy

For the development of catalytic materials employing nanoparticles (NPs), understanding the different reactivity of the nanoparticle surfaces and facets is a topic of constant research. For example, Pt NPs are used in the automotive

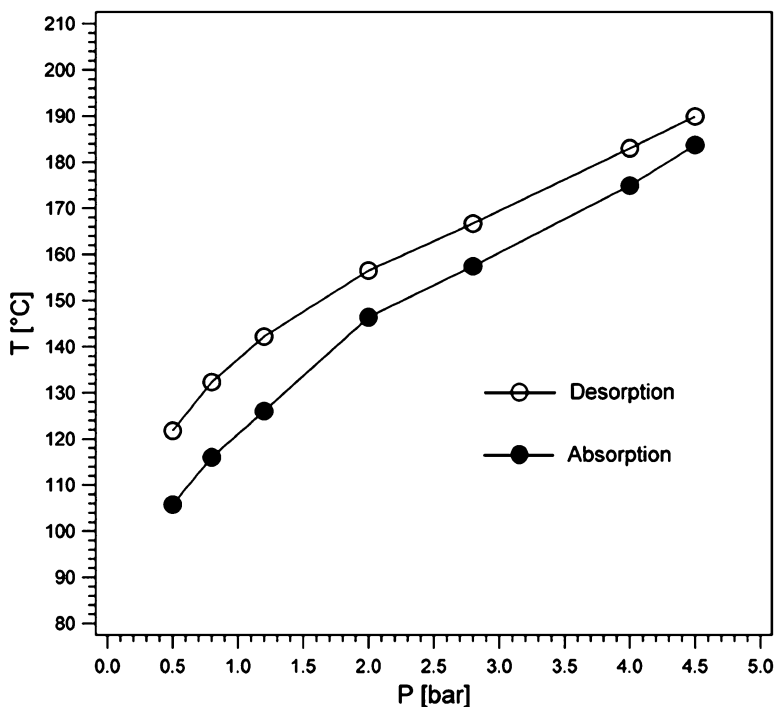


Fig. 6.26 Hydrogen absorption and desorption temperatures as a function of H_2 pressure. A hysteresis is visible between transformations upon a decrease of T (absorption) and an increase of T (desorption)

industries for the catalytic conversion of CO to CO_2 to control unwanted CO emission. The behavior of Pt catalyst NPs in a dynamic environment is also dynamic as the result of the changing free energy of the NPs surfaces with gas composition (Newton et al. 2007). Vendelbo et al. (2014) studied this behavior by in situ TEM using the all-in-one NR described above in Sect. 6.8.6.

The catalyst Pt NPs with 3–30 nm diameters were prepared by impregnation of an NR with an aqueous solution of tetraammineplatinum(II)nitrate followed by calcination in air at 573 K. A gas mixture of CO , O_2 , and He (4.2 %:21.0 %:74.8 %) flowed through the NR containing the NPs into a mass spectrometer to analyze the reaction products, see Fig. 6.27. The reaction taking place at the NPs in the reaction zone is described as:

- $CO(g) + * \rightarrow CO^*$
- $O_2(g) + * \rightarrow O_2^*$
- $O_2^* + * \rightarrow 2O^*$
- $CO^* + O^* \rightarrow CO_2(g) + 2^*$

where $*$ denotes a free surface site on a catalytic NP, and X^* denotes an adsorbed species. The temperature in the reaction zone was increased to a nominal value of

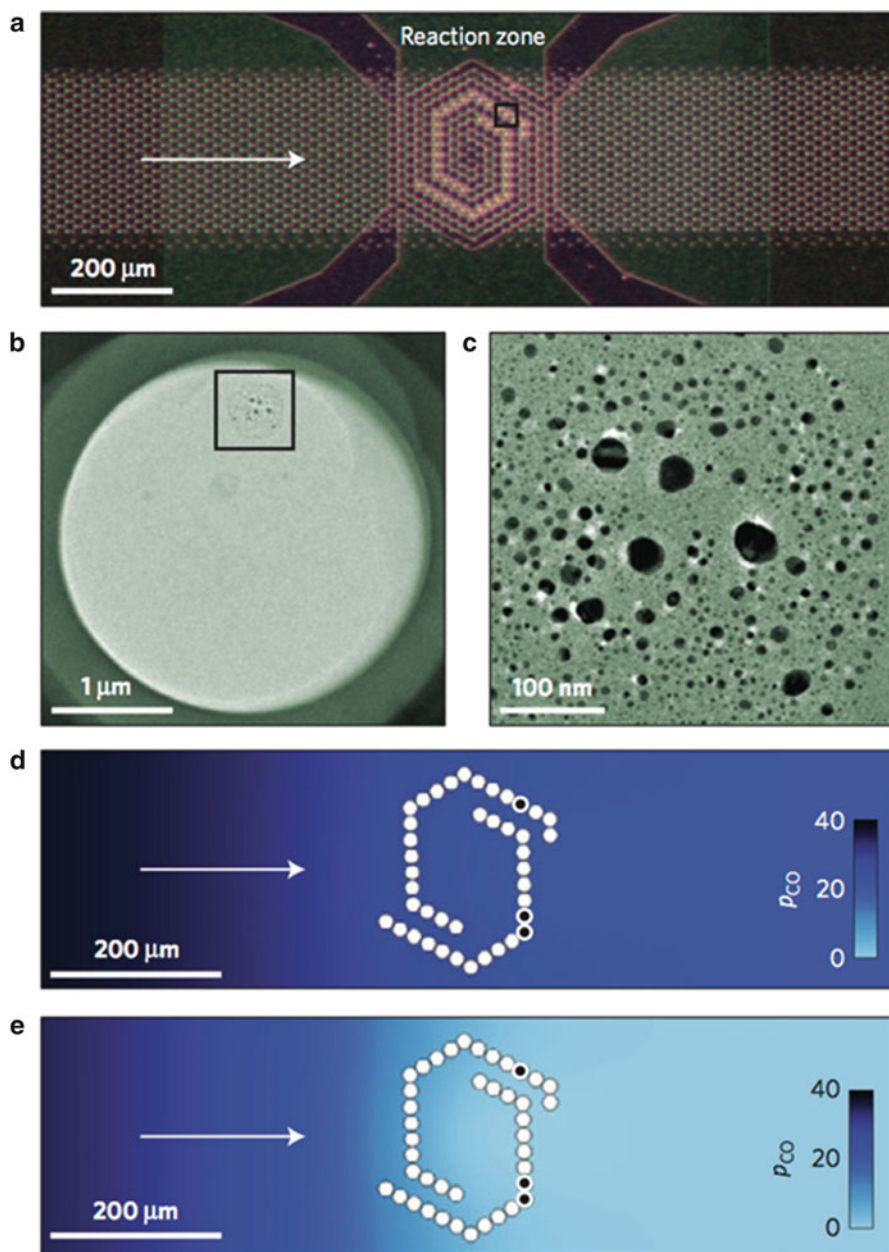


Fig. 6.27 (a) Light optical micrograph of the nanoreactor with the gas channel and the reaction zone including the heater spiral and electron transparent windows. (b) An electron micrograph of the framed window in a showing that Pt nanoparticles (*dark contrast*) are dispersed heterogeneously on the electron transparent windows (uniform, bright contrast). (c) An electron micrograph showing a close-up of the as-prepared Pt nanoparticles framed in (b). (d, e) Steady-state simulation of the CO concentration profile ($[p_{\text{CO}}]$: mbar) in the nanoreactor for the low conversion branch of the bistable regime at 710 K (d) and the high conversion branch of the bistable regime at 710 K (e). The *arrow* in (a, d, e) indicates the gas-flow direction. White discs superimposed on (d, e) indicates the positions of the electron transparent windows

710 K (total power input ~ 19 mW), and CO_2 was recorded in the spectrometer. The concentrations of CO_2 and CO started to fluctuate periodically spontaneously, or by a minor temperature change of 0.5–1.0 K, and were observed at temperatures in the range 659–729 K. During the oscillating reaction, the average NR temperature was kept constant by compensating the exothermic reaction heat with a reduction in the heater power. (Hence the heater power changes reflect the changes in the reactions taking place, with a faster response time as the pressure changes dampened by the tube system.)

At the same time as the spectrometer recorded the reaction product concentrations, images were recorded of NPs at a specific position in the reaction zone. At the inlet of the reaction zone, the NPs were observed to be static and more or less rounded in shape. In contrast, near the reaction zone outlet, the Pt nanoparticles switched between a more spherical and a more faceted morphology. In Fig. 6.28, the oscillations in gas pressures are demonstrated together with the morphology changes of a Pt NP near the outlet. It turns out that the morphology changes from spherical to more faceted and back is synchronous with the pressure oscillations. A high conversion is associated with a transformation towards low index Pt NP facets like $\{111\}$, while a lower conversion is associated with a conversion to high index facets.

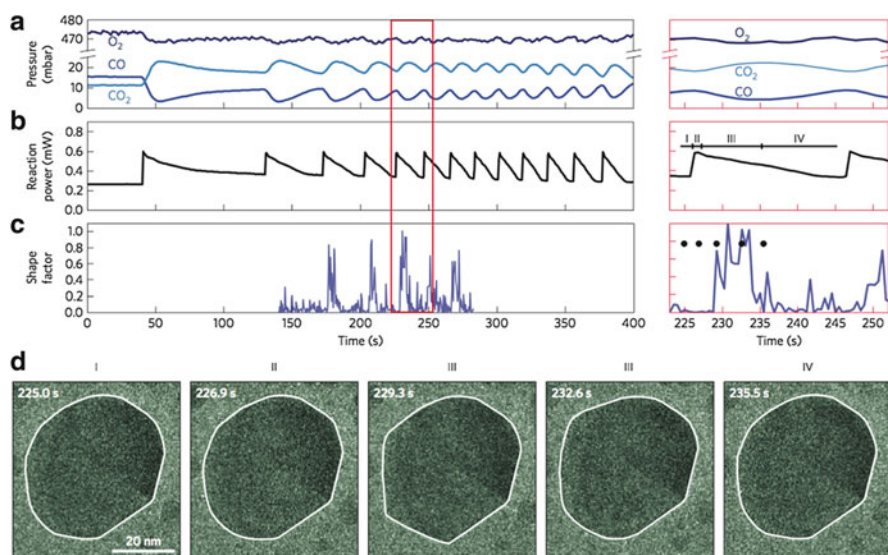


Fig. 6.28 Oscillatory CO oxidation reaction data correlated with the projected morphology changes of a Pt nanoparticle. The gas entering the reaction zone is 1.0 bar of $\text{CO}:\text{O}_2:\text{He}$ at 3%:42%:55% and NR temperature is 659 K. (a–c) Mass spectrometry of the CO , O_2 , and CO_2 pressures (a), reaction power (b), and shape factor (c) for the Pt nanoparticle in d as a function of time. The shape factor corresponds to the relative difference in area from the best elliptical fit in image I in (d). The morphology factor is zero for the more spherical shape and deviates for more faceted particles. Part of the reaction oscillation data is highlighted by the red rectangle

Thus, the individual NPs near the exit from the reaction zone can undergo oscillatory and reversible shape changes with a temporal frequency matching the oscillations in reaction power, indicating that the oscillatory CO conversion and the dynamic shape change of the Pt NPs are coupled. This behavior was rationalized with a micro kinetic model using DFT calculations of the Pt surface CO and O adsorption and transition state energies, taking into account the CO pressure variation across the reaction zone. It showed that at higher CO pressures more open surfaces (high index planes like {112}) show a high CO coverage, and is stabilized, resulting in more rounded (high index surfaces) NP morphologies, as observed near the inlet, where the CO concentration is high. At lower CO pressures, the low index facets are stabilized with respect to the more open surfaces. Taking into account the flow in the NR and the morphology change rate proportional to the deviation from the equilibrium shape, an oscillatory pressure behavior coupled to periodic morphology variations could be described.

6.10.3 Corrosion and Heat-Treatment in Al Alloys

One of the applications of the NR is to understand a common metallurgical problem of localized corrosion. For example, aluminum alloys are generally considered corrosion resistive, but localized corrosion can arise from micro-galvanic couples due to extremely fine, nanometer, size precipitates, and solute depleted regions. The distribution of precipitates and solute depleted regions varies depending on the heat-treatment given to the alloys. Investigating the corrosion at the nanoscale is extremely challenging using conventional electrochemical methods. In such cases, in situ TEM studies using NR plays an important role in not just giving an understanding of the corrosion mechanisms at a submicron scale, but also on the influence of heat-treatments on the microstructural change and corrosion behavior of these alloys.

For carrying out corrosion studies inside the TEM, it is important to identify the four components of a corrosion cell: anode, cathode, conducting path and electrolyte. Due to the large density of precipitates and solute depleted zones inside the alloy, there are numerous anodes, cathodes connected by a conducting path (the Al matrix). In the presence of a suitable electrolyte, this system acts as a spontaneous corrosion cell. In order to identify an electrolyte suitable for in situ TEM studies, ex situ and quasi in situ experiments have been carried out. An aerosol of oxygen bubbled through aqueous HCl (pH=3) has been identified to cause localized corrosion attack in reasonably short time for TEM investigation.

The specimens for in situ TEM studies (Malladi et al. 2013) are prepared using a focused ion beam (FIB). Using a dual-beam SEM/FIB, cross-sectional specimens of dimensions $15\ \mu\text{m} \times 5\ \mu\text{m} \times 100\ \text{nm}$ are prepared across grain boundaries and other areas prone to localized corrosive attack. The specimens are then transferred to the bottom chip of the NR, which also consists of an embedded Pt heater. Upon

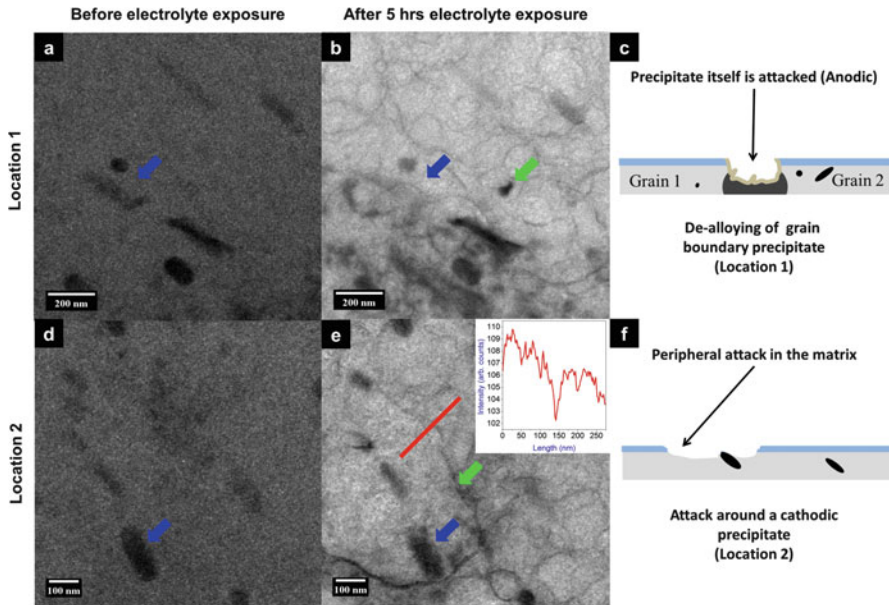


Fig. 6.29 (a–c) De-alloying of an anodic grain-boundary precipitate and (d–f), peripheral attack around cathodic matrix precipitates

combining with the top chip, the NR is assembled. The NR is placed in the flow-gas holder and introduced into the TEM for in situ TEM investigations.

Figure 6.29 shows snapshots from a movie recorded while exposing an FIB specimen of aluminum alloy AA2024-T3 to oxygen bubbled through aqueous HCl. The gas mixture was maintained at a pressure of 1 bar, and the specimen was maintained at room temperature. The bright-field TEM images from two areas of the FIB specimen show two kinds of localized corrosion attack. The location 1 (Fig. 6.29a–c) corresponds to the corrosion attack of an anodic grain-boundary precipitate. After exposing to the electrolyte for 5 h, the intensity of the grain-boundary precipitate indicated by the blue arrow diminishes significantly. EDX compositional analysis on several specimens of this alloy showed that the grain-boundary precipitates have been enriched in Mg, indicating the anodic nature of the attack. Likewise in location 2, an attack on the matrix surrounding platelet-like matrix precipitates was identified as an attack around cathodic precipitates. The precipitates have been identified as precipitates containing Cu, Mn, Fe, and Si. These two types of attacks are the origins of localized corrosion in Al alloys.

Most of the Al alloys have the unique property of improving their strength by the mechanism known as precipitation hardening. This involves a special heat-treatment given to the alloys where alloying elements are added to aluminum, heated to an elevated temperature (usually above 500 °C) to form a single-phase solid solution, and then quenched rapidly to room temperature.

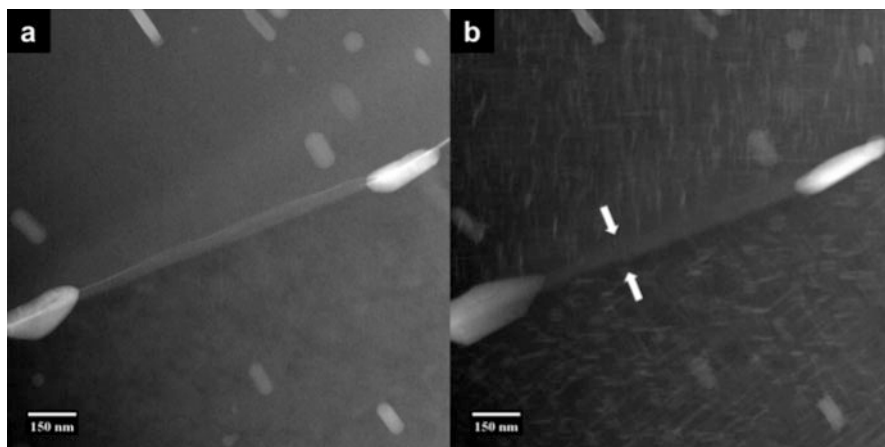


Fig. 6.30 STEM-annular dark-field images obtained from an FIB specimen of AA2024 (a) before and (b) after heat-treatment at 250 °C for 3 min. Prior to heat-treatment, there exist numerous matrix precipitates enriched in Mn, Cu, Fe, and Si, whereas heat-treatment results in precipitation of fine nanometer-sized S-type precipitates enriched in Cu and Mg. Also notice the precipitate-free zone indicated by the *arrows* next to the grain boundary

On quenching, a super-saturated solid solution is obtained, from which a distribution of numerous fine nano-sized precipitates in the matrix can be obtained by heating at slightly elevated temperatures (typically ranging from 100 to 250 °C). Fig. 6.30 shows the precipitation of numerous S-type nano-precipitates in the matrix of an FIB specimen of AA2024, heat-treated at 250 °C for 3 min. While the formation of the S-type precipitates contributes to a significant increase in the strength of the alloy, the Mg-rich S-type precipitates and the formation of precipitate-free zones next to the grain boundary have a severely detrimental effect on the corrosion behavior of this alloy.

The corrosion behavior of the heat-treated specimen can be investigated by assembling an NR and carrying out in situ corrosion experiments as described previously. The heat-treated specimen was also exposed to a gas mixture of oxygen bubbled through aqueous HCl at room temperature, at a pressure of 1 bar. The snapshots from a movie recorded during the in situ corrosion experiment are shown in Fig. 6.31. In contrast to the specimen prior to heat-treatment, Fig. 6.29, exposure to the reactive gas mixture of oxygen bubbled through aqueous HCl causes an immediate attack as shown in Fig. 6.29a. The bubble-like features observed all over the specimen indicate this, and more prominently next to the grain-boundary precipitates. As the exposure time increases, the corrosion attack progresses as observed by the growth of circular features all over the matrix after exposure of 15 min (Fig. 6.31b) and approximately 30 min (Fig. 6.31c). STEM-ADF tilt series confirms that the circular feature observed all over the specimen are pits initiating from the surface of the sample. The high density of the S-type precipitates enriched in Mg and Cu acts as numerous galvanic couples leading to such an attack. More

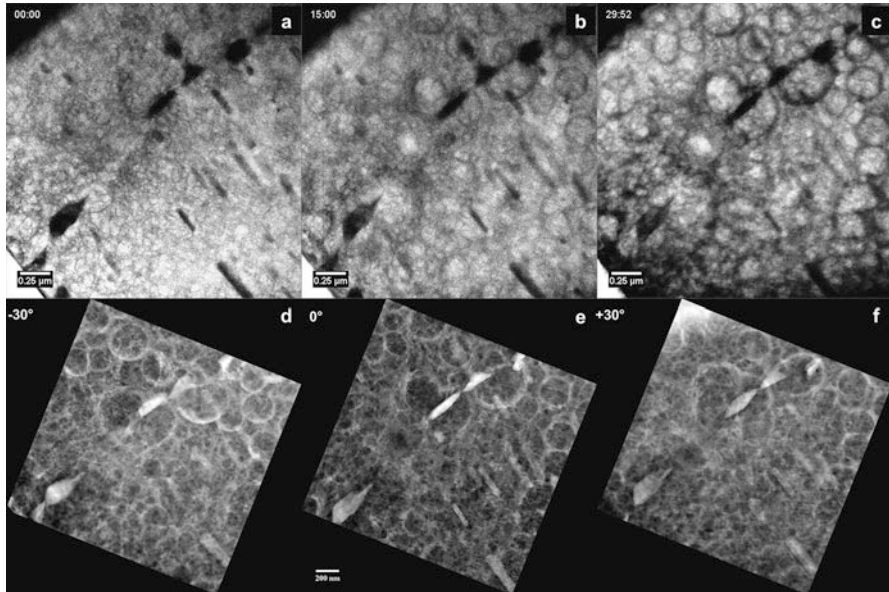


Fig. 6.31 (a) Surface attack and selective attack next to grain-boundary precipitates in a heat-treated FIB specimen of AA2024. The surface attack progresses rapidly after (b) 15 min, as indicated by the increase in the size of the circular features. The attack progresses more and the whole specimen surface is attacked after (c) at approximately 30 min. Projections at (d) -30° , (e) 0° , and (f) $+30^\circ$ from STEM-ADF tilt series obtained from the region shows that the *circular* features are in fact pits formed due to the corrosive attack

studies on understanding the propagation of corrosive attack by correlating with compositional analysis and other combinations of heat-treatment and corrosion are in progress.

Acknowledgements For the cleanroom work in fabricating the nanoreactors and various experiments, we acknowledge G. Pandraud, T. Alan, and L. Vicarelli. For the mechanical machining, we acknowledge T.R. de Kruijff, A. Grafhorst, L. van Luijk, and M. Camp.

The authors gratefully acknowledge the ERC project “In situ NanoElectrical Measurements in a Transmission Electron Microscope” (TSIC 69) for support.

References

- T. Alan, P.M. Sarro, A comparative study of the strength of Si, SiN and SiC used at nanoscales. *Mater. Res. Soc. Symp.* P **1052**, 241–245 (2008)
- T. Alan, M.A. Hines, A.T. Zehnder, Effect of surface morphology on the fracture strength of silicon nanobeams. *Appl. Phys. Lett.* **89**(9) (2006)
- T. Alan, J. Gaspar, O. Paul, H.W. Zandbergen, F. Creemer, PM Sarro, Characterization of ultrathin membranes to enable TEM observation of gas reactions at high pressures, in *ASME 2009*

- International Mechanical Engineering Congress and Exposition* (American Society of Mechanical Engineers, 2009), pp 327–331
- T. Alan, T. Yokosawa, J. Gaspar, G. Pandraud, O. Paul, F. Creemer, P.M. Sarro, H.W. Zandbergen, Micro-fabricated channel with ultra-thin yet ultra-strong windows enables electron microscopy under 4-bar pressure. *Appl. Phys. Lett.* **100**(8) (2012)
- F. Banhart, Irradiation effects in carbon nanostructures. *Rep. Prog. Phys.* **62**(8), 1181–1221 (1999)
- J.F. Creemer, S. Helveg, G.H. Hovelings, S. Ullmann, A.M. Molenbroek, P.M. Sarro, H.W. Zandbergen, Atomic-scale electron microscopy at ambient pressure. *Ultramicroscopy* **108**(9), 993–998 (2008). doi:[10.1016/j.ultramicro.2008.04.014](https://doi.org/10.1016/j.ultramicro.2008.04.014)
- J. Creemer, F. Santagata, B. Morana, L. Mele, T. Alan, E. Iervolino, G. Pandraud, P. Sarro, An all-in-one nanoreactor for high-resolution microscopy on nanomaterials at high pressures, in *Micro Electro Mechanical Systems (MEMS), 2011 I.E. 24th International Conference on, 2011* (IEEE, 2011), pp. 1103–1106
- N. de Jonge, F.M. Ross, Electron microscopy of specimens in liquid. *Nat. Nanotechnol.* **6**(11), 695–704 (2011)
- N. de Jonge, M. Pfaffa, D.B. Peckysa, Practical aspects of transmission electron microscopy in liquid. *Adv. Imag. Electron Phys.* **186**, 1–37 (2014)
- R.F. Egerton, P. Li, M. Malac, Radiation damage in the TEM and SEM. *Micron* **35**(6), 399–409 (2004). doi:[10.1016/j.micron.2004.02.003](https://doi.org/10.1016/j.micron.2004.02.003)
- H. Ghassemi, W. Harlow, O. Mashtalir, M. Beidaghi, M.R. Lukatskaya, Y. Gogotsi, M.L. Taheri, In situ environmental transmission electron microscopy study of oxidation of two-dimensional Ti_3C_2 and formation of carbon-supported TiO_2 . *J. Mater. Chem. A* **2**(35), 14339–14343 (2014)
- Y.N. Guo, J. Zou, M. Paladugu, H. Wang, Q. Gao, H.H. Tan, C. Jagadish, Structural characteristics of GaSb/GaAs nanowire heterostructures grown by metal-organic chemical vapor deposition. *Appl. Phys. Lett.* **89**(23), 231917 (2006). doi:[10.1063/1.2402234](https://doi.org/10.1063/1.2402234)
- T.R. Hart, R.L. Aggarwal, B. Lax, Temperature dependence of Raman scattering in silicon. *Phys. Rev. B Solid St* **1**(2), 638 (1970)
- L. He, R. Hull, Quantification of electron-phonon scattering for determination of temperature variations at high spatial resolution in the transmission electron microscope. *Nanotechnology* **23**(20), 205705 (2012). doi:[10.1088/0957-4484/23/20/205705](https://doi.org/10.1088/0957-4484/23/20/205705)
- M.E. Holtz, Y.C. Yu, D. Gunceler, J. Gao, R. Sundararaman, K.A. Schwarz, T.A. Arias, H.D. Abruna, D.A. Muller, Nanoscale imaging of lithium ion distribution during in situ operation of battery electrode and electrolyte. *Nano Lett.* **14**(3), 1453–1459 (2014)
- F.M. Huang, K.T. Yue, P.H. Tan, S.L. Zhang, Z.J. Shi, X.H. Zhou, Z.N. Gu, Temperature dependence of the Raman spectra of carbon nanotubes. *J. Appl. Phys.* **84**(7), 4022–4024 (1998)
- A. Jenichen, C. Engler, Metal-organic chemical vapour deposition of (BInGa)P: density-functional calculations to the mechanisms. *J. Cryst. Growth* **312**(1), 10–15 (2009). doi:[10.1016/j.jcrysgro.2009.10.001](https://doi.org/10.1016/j.jcrysgro.2009.10.001)
- J.M. López Nieto, P. Botella, B. Solsona, J.M. Oliver, The selective oxidation of propane on Mo-V-Te-Nb-O catalysts. *Catal. Today* **81**(2), 87–94 (2003). doi:[10.1016/s0920-5861\(03\)00119-6](https://doi.org/10.1016/s0920-5861(03)00119-6)
- S. Malladi, C.G. Shen, Q. Xu, T. de Kruijff, E. Yucelen, F. Tichelaar, H. Zandbergen, Localised corrosion in aluminium alloy 2024-T3 using in situ TEM. *Chem. Commun.* **49**(92), 10859–10861 (2013)
- M.A. Newton, C. Belver-Coldeira, A. Martinez-Arias, M. Fernandez-Garcia, Dynamic in situ observation of rapid size and shape change of supported Pd nanoparticles during CO/NO cycling. *Nat. Mater.* **6**(7), 528–532 (2007)
- M.H. Nielsen, S. Aloni, J.J. De Yoreo, In situ TEM imaging of CaCO_3 nucleation reveals coexistence of direct and indirect pathways. *Science* **345**(6201), 1158–1162 (2014)
- O. Paul, J. Gaspar, *Thin-Film Characterization Using the Bulge Test. Reliability of MEMS* (Wiley-VCH, Weinheim, 2008), pp. 67–121. doi:[10.1002/9783527622139.ch3](https://doi.org/10.1002/9783527622139.ch3)

- S. Qian, D.O. Northwood, Hysteresis in metal hydrogen systems—a critical-review of the experimental-observations and theoretical-models. *Int. J. Hydrogen Energy* **13**(1), 25–35 (1988)
- A. Radisic, P.M. Vereecken, J.B. Hannon, P.C. Searson, F.M. Ross, Quantifying electrochemical nucleation and growth of nanoscale clusters using real-time kinetic data. *Nano Lett.* **6**(2), 238–242 (2006)
- B. Song, G.F. Schneider, Q. Xu, G. Pandraud, C. Dekker, H. Zandbergen, Atomic-scale electron-beam sculpting of near-defect-free graphene nanostructures. *Nano Lett.* **11**(6), 2247–2250 (2011)
- A.J. Storm, J.H. Chen, X.S. Ling, H.W. Zandbergen, C. Dekker, Fabrication of solid-state nanopores with single-nanometre precision. *Nat. Mater.* **2**(8), 537–540 (2003)
- T. Tsuchiya, O. Tabata, J. Sakata, Y. Taga, Specimen size effect of tensile strength of surface-micromachined polycrystalline silicon thin films. *J. Microelectromech. S* **7**(1), 106–113 (1998)
- S.B. Vendelbo, C.F. Elkjaer, H. Falsig, I. Puspitasari, P. Dona, L. Mele, B. Morana, B.J. Nelissen, R. van Rijn, J.F. Creemer, P.J. Kooyman, S. Helveg, Visualization of oscillatory behaviour of Pt nanoparticles catalysing CO oxidation. *Nat. Mater.* **13**(9), 884–890 (2014). doi:[10.1038/NMAT4033](https://doi.org/10.1038/NMAT4033)
- M.Y. Wu, D. Krapf, M. Zandbergen, H. Zandbergen, P.E. Batson, Formation of nanopores in a SiN/SiO₂ membrane with an electron beam. *Appl. Phys. Lett.* **87**(11) (2005)
- H.L.L. Xin, K.Y. Niu, D.H. Alsem, H.M. Zheng, In situ TEM study of catalytic nanoparticle reactions in atmospheric pressure gas environment. *Microsc. Microanal.* **19**(6), 1558–1568 (2013)
- A.O. Yalcin, B. de Nijs, Z.C. Fan, F.D. Tichelaar, D. Vanmaekelbergh, A. van Blaaderen, T.J.H. Vlugt, M.A. van Huis, H.W. Zandbergen, Core-shell reconfiguration through thermal annealing in Fe_xO/CoFe₂O₄ ordered 2D nanocrystal arrays. *Nanotechnology* **25**(5) (2014)
- T. Yokosawa, T. Alan, G. Pandraud, B. Dam, H. Zandbergen, In-situ TEM on (de)hydrogenation of Pd at 0.5–4.5 bar hydrogen pressure and 20–400 degrees C. *Ultramicroscopy* **112**(1), 47–52 (2012)
- N.P. Young, M.A. van Huis, H.W. Zandbergen, H. Xu, A.I. Kirkland, Transformations of gold nanoparticles investigated using variable temperature high-resolution transmission electron microscopy. *Ultramicroscopy* **110**(5), 506–516 (2010)
- G.Z. Zhu, S. Prabhudev, J. Yang, C.M. Gabardo, G.A. Botton, L. Soleymani, In situ liquid cell TEM study of morphological evolution and degradation of Pt-Fe nanocatalysts during potential cycling. *J. Phys. Chem. C* **118**(38), 22111–22119 (2014)